Buckling Free and High Optical Quality Factor Large Thin Rib Disk

by

Shahin Honari

B.Sc., Sharif University of Technology, 2014

M.Sc., University of Texas at Dallas, 2018

A Dissertation Submitted in Partial Fulfillment of the

Requirements for the Degree of

DOCTOR OF PHILOSOPHY

in the Department of Electrical and Computer Engineering

Buckling Free and High Optical Quality Factor Large Thin Rib Disk

by

Shahin Honari

B.Sc., Sharif University of Technology, 2014

M.Sc., University of Texas at Dallas, 2018

Supervisory Committee

Dr. Tao Lu, Supervisor

(Department of Electrical and Computer Engineering)

Dr. Chris Papadopoulos, Departmental Member

(Department of Electrical and Computer Engineering)

Dr. Rodney Herring, Outside of Department Member

(Department of Mechanical Engineering)

ABSTRACT

This thesis investigates the fabrication and characterization of Silica on Silicon (SoS) microcavities, for potential comb generation and sensing applications. In this thesis, novel approaches were introduced on silica-on-silicon microdisks to remove some of the inherent hurdles, namely mitigating the rough surface through chemo-mechanical polishing, and suppressing buckling-induced mechanical instability by introducing a rib disk structure. Quality factors as high as 10^8 were achieved for polished disks. Furthermore using the rib-disk structure, microdisks with thickness smaller than $1.5\mu m$ and quality factors as high as 10^7 materialized. By addressing these challenges we unleash the enormous potentials of ultra-high Q silica microdisks in microcomb generation in visible regime and sensing. Finally, a multi-transverse mode dense comb generation scheme on this platform is investigated.

Contents

Supervisory Committee **ii**

Table of Contents **iv**

List of Figures **vi**

Acknowledgment **xiii**

Dedication **xiv**

1 Introduction **1**

1.1 Research Overview 1

1.2 Contributions 4

1.3 Outline 4

2 Whispering Gallery Mode Microcavities **6**

2.1 Different Types of WGM Microcavities 7

2.2 Materials for WGM Microcavity Fabrication 8

2.3 Optical Quality Factor (Q) 9

2.4 Mode Volume 11

2.5 Measurement Setup 12

2.6 Dispersion 14

2.7 Geometrical Considerations of Dispersion 17

2.8 Material Dispersion 18

3 Microcomb Generation 26

3.1 Soliton Microcombs 27

3.2 Visible Wavelength Comb Generation 29

3.3 Analytical Description of Soliton 31

4 Fabrication of Ultra-High Q Silica Microdisk Using Chemo-Mechanical Polishing 41

4.1 Chemo-Mechanical Polishing 51

5 A Novel Buckle-Free Large Rib Microdisk with Sub-Micron Thickness 53

5.1 Buckling Simulation 59

6 Frequency Comb Generation in Short Wavelengths 62

7 Summary and Future Works 74

Bibliography 79

List of Figures

Figure 2.1 a) Microdisk, b) Microring [1], c) Microtoroid [2], d) Microsphere [3], e) Cylindrical microresonator [4], and f) Microbubble resonator [5] 19

Figure 2.2 Q measurements for red detuned a), and blue-detuned b) scan with the associated Lorezian fit. The slight difference between the total Q (Q_t), and the intrinsic Q (Q_i) is because of the coupling loss 20

Figure 2.3 Cylindrical coordinates of a disk with the tapred fiber on top [6] 20

Figure 2.4 a) and b), intensity of the TE polarized WGM mode in microdisks with different thickness, c) E_r and d) H_r fields distribution for $LiNbO_3$ microdisks. 21

Figure 2.5 The light coupling apparatus for our microdisks, a)fiber holder on the stage b) the torch used for fiber pulling 21

Figure 2.6 The schematic of a Q measuring setup. The ice water would be added to minimize the temperature fluctuation's effect on the interferometer, the polarization controllers enable us to achieve maximum coupling [7] 22

Figure 2.7 Optical measurement setup 23

Figure 2.8 Mach-Zender interferometer schematic [8] 24

Figure 2.9 Simulated D_{int} and β_2 in 1300 nm- 1800 nm range for the fundamental TE mode of the 1mm rib disk in [9]. The D_{int} is shown in a) as a function of azimuthal mode number away from the center wavelength of 1550 nm, and b) is the associated β_2 for the same wavelength window. β_2 of water is included in b) as a reference to a different medium 24

Figure 2.10The simulated D_{int}(a) and D(b) vs frequency and wavelength of a microdisk with 6 μm thickness and 300 μm of radius [10]. Copyright, 2020 De Gruyter 24

Figure 2.11The simulated D_{int}(a) and D(b) vs frequency and wavelength of a microdisk with a fixed wedge angle and 300 μm of radius [10]. Copyright, 2020 De Gruyter 25

Figure 2.12Dispersion for four different materials vs wavelength [10]. Copyright 2022, De Gruyter 25

Figure 3.1 Left: SCG of microcomb using a dispersion-engineered waveguide and a mode-locked laser, ultra-short pulses would expand in the spectrum upon passing through the waveguide, with spacing determined by the repetition rate. Right: KCG of microcomb using a CW laser and a dispersion-engineered microresonator, with spacing determined by the FSR of the microresonator [11]. Copyright, 2019 Nature Publishing Group 27

Figure 3.2 a) Spectrum of parametric frequency conversion observed in a microsphere pumped at 1550 nm, units of dBm represents a logarithmic power relative to power of 1mW, b) Schematic of a degenerate (left) and non-degenerate (right) FWM among cavity eigenmodes, c) SEM image of a silica microsphere. 37

Figure 3.3 Bistability curve shows how the intracavity power changes with laser detuning in a normal resonator (blue curve), and in the presence of thermal effects on the resonance (orange). The increase in temperature in the cavity can move the resonance peak to higher wavelengths, so the Lorenzian shape of the resonance peak will change to a triangle like shape. The left inset shows an FWM comb where the comb lines can remain out of phase, and the right inset shows the soliton generation where comb lines are in phase and synchronized, with a pulsed-like intracavity power. copyright 2014, Nature Publishing Group [12] 38

Figure 3.4 The bistability curve showing the steps of soliton generation. The upper branch is effectively blue-detuned and the lower branch is effectively red-detuned. When moving the laser from shorter to longer wavelengths, the intracavity power follows the upper branch of the bistability curve, until it hits a certain value and drops to the lower branch. copyright 2018, The Royal Society Publishing [13] 39

Figure 3.5 Calculated second-order dispersion for two hybridized mode families at different silica microdisk thicknesses. The blue curve shows anomalous dispersion [14]. Copyright Nature Publishing Group, 2017 39

Figure 3.6 The comb generated in water via AMX in near visible wavelength range. B), d) and f) are the comb generated from the pump shown in a), c) and e) respectively. Note that the eigenfrequencies dramatically change and Q degrades when AMX happens. Copyright Optica Publishing Group, 2022 [15] 40

Figure 3.7 AMX for TE00 and TM00 mode families for the microring structure in [16]. As can be seen the local dispersion changes from normal to strong anomalous due to AMX for the TE00 mode, Copyright Nature Publishing Group, 2018 40

Figure 4.1 Fabrication procedure: (a) photolithography of the resist to transfer the pattern, (b) HF wet etch to make the disk, (c) CMP step to increase the smoothness of the surface, and (d) etching Si substrate to make the pillar. 43

Figure 4.2 Normalized transmission spectra of a 1 mm disk at a whispering gallery mode around $\lambda = 971.32\ nm$ are displayed in (a) and (b). (c) Intrinsic Q as a function of disk diameter at 970 nm (blue squares), 1550 nm (red squares) wavelength bands with the lengths of the error bars corresponding to the differences of the measured intrinsic Q at red and blue detune. In comparison, the recorded values of 7.5 μm and 10 μm thick microdisks by Lee et. al. [17] are displayed as green squares. Note that, after polishing, the silica thin film thickness of our disks reduced from 10 μm to 7.5 μm. (d) The side view SEM micrograph of a polished disk. (e) The top-view micrograph further confirms the upper edge between the side wall and top surface vanishes after polish as opposed to the visible upper edge of an unpolished disk displayed in (f). The atomic force microscope (AFM) micrographs of (g) the edge of a polished disk, (h) the edge of an unpolished disk and (i) the top surface of an unpolished disk show the RMS values of roughness are 0.45 nm, 1.09 nm and 0.33 nm respectively. The black bars on e-f represent 400 nm. 45

Figure 4.3 Intrinsic Q at 635 nm (blue circles), 970 nm (green squares), and 1550 nm (red triangles), measured before annealing, within 15 minutes after annealing, and 4 days after annealing. 48

Figure 5.1 A 3-D model of a) the proposed rib disk and b) a regular disk. The top view micrograph c) shows no buckling on the rib disk edge while d) the regular disk with the same undercut ratio is severely buckled. Plot e) further shows the top view SEM of the rib disk. The width of the disk rib is around 20 μm. f) is the SEM image of a buckled regular disk. The AFM images at g) and h) show the surface roughness of the top part and the rib part of the rib disk respectively, RMS values obtained for each part is shown in the figure. Roughness RMS is 0.33 nm for the top part and 0.39 nm for the rib part. i), j), and k) are the fabrication steps of the rib disk. The white bars on optical microscope images are 50 μm each. 55

Figure 5.2 a) A side-view SEM image of a rib disk along with the simulated mode profile (inset), The thickness of the rib and top part of the disk were calculated after accounting for a slight slope of the sample. The graph at b) represents optical Q data for two different wavelengths with the normalized transmission spectrum in the inset. The white bar in the SEM image is 20 μm in length. 57

Figure 5.3 a) Buckling threshold for rib and regular disk as a function of disk radius (R_D) and the undercut ratio ξ. The yellow-coloured region in the graph represents the gain in our design, where the rib disk remains mechanically stable, but the regular disk with the same dimensions and undercut buckles, while in the blue-coloured region, both structures show buckling. At the setting ("x" marker), where both disks were fabricated, the simulation b) shows that a regular disk will buckle while a rib disk showing in c) will not buckle. 59

Figure 6.1 The profilometer data showing the side view of the rib disk for 12 minutes polish (top), and 15 minutes polish (bottom), used to simulate the modes 64

Figure 6.2 Comb lines generated in a rib disk through FWM process, in the air(a), and DPBS solution (b). The spacing in both cases is about 0.01 nm 67

Figure 6.3 Modes responsible for comb line generation in the air (top), and in DPBS(bottom) with the observed 0.01 nm spacing 68

Figure 6.4 Same as 6.3, but for ω vs azimuthal mode order. The top image is for modes generated in the air and the bottom image is for the modes generated in water 69

Figure 6.5 Q measurements in the air (top) and in DPBS solution (bottom). the measurements confrim high quality factors can be achieved in both media using the rib disk. 70

Figure 6.6 The modes responsible for the curve found in Fig. 6.3 in DPBS, the azimuthal mode number increasing does not remain constant. This can be explained by the difference in the angle of momentum for different transverse mode families. 71

Figure 6.7 The optical setup used for comb generation and Q measurements, a tunable laser is amplified at 1550 nm wavelength, and a $LiNbO_3$ frequency doubler is used to generate 775 nm wavelength. The light is coupled to the rib disk through a tapered fiber. 72

ACKNOWLEDGMENT

I would like to thank Dr Tao Lu for his support and guidance throughout my work at UVic. Dr Lu's passion and supervision was integral to the success I had in conducting research. I would also like to appreciate Dr Chris Papadopoulos and Dr Rodney Herring for their valuable input and support as members of my supervisory committee. I would like to extend my appreciation to Mr Jon Rudge, Dr. Elaine Humphrey, and all the staff at CAMTEC and AMF centers at UVic for their support and training provided on nanofabrication and microscopy facilities. Finally I want to thank other members of Dr Lu's lab specially Saeed Farajollahi, who helped a lot in the simulation part of my work, Guoliang Li, and Sanaul Haque, who helped me with the setup and some measurements.

To my family; Nilou, Nasrin, Hormoz, Shervin and Arvin

Chapter 1

Introduction

1.1 Research Overview

Silica is one of the most abundant materials on the earth. Furthermore, the low-loss nature of the silica film, along with relative ease of growth on the silicon platform, makes it an ideal candidate for photonic devices and lab-on-chip concept devices. Hence, there has been a lot of interest lately in trying to incorporate silica microcavities into the existing complementary metal-oxide-semiconductor (CMOS) fabrication processes and technologies. Optical microcavities are purposefully structured devices, able to confine the light in small spaces. These devices are designed to concentrate light into a small volume using resonant circulation [18]. The light confinement happens as a result of low optical loss nature of the microcavity and is characterized by quality factor (Q) parameter. This parameter, shows how well light can circulate inside a microcavity at resonance without loss. Ultra-high Q microcavities with Qs above one billion were observed [19, 20, 21, 22], using different materials. However, there is a great interest in SiO_2 microcavities because of the low optical loss of silica in visible to near-infrared regime, relatively easy growth process on Si, and compatibility

with existing CMOS fabrication processes [23, 24]. Among different kinds of optical microcavities, WGM (Whispering Gallery Mode) microcavities have been some of the hottest areas of research studies lately. These microcavities are at the forefront of many studies in different fields ranging from nanoparticle sensing [7, 25, 26] to comb generation [14, 27, 2].

Frequency microcomb generation is one of the numerous capabilities of silica microcavities. An optical microcomb is a set of equidistant frequency markers [2, 28], which finds numerous applications across different fields, especially in sensing and spectroscopy, timekeeping, and distance ranging [11, 29]. Although initially observed using mode-locked lasers [28], microcomb generation has significantly affected WGM microcavity-related research studies lately [14, 30, 31]. The comb generation happens because of a nonlinear interaction in the medium (Kerr nonlinearity), and the spectrum extends beyond the pump wavelength by a parametric four-wave mixing (FWM) process [11]. This process like any other transition needs momentum and energy to be conserved. Hence, it is critical to have a better understanding of the details of the FWM process. In a WGM microcavity, the optical modes are angular momentum eigenstates with propagation constant $\beta_m \approx m/R$, where m is the azimuthal mode order and R is the radius of the cavity. Therefore, the conversion of two photons from the pump laser into two photons with higher and lower mode orders, will conserve the momentum naturally [2]. The energy of the two photons created is proportional to the frequency of the two adjacent modes. So, the energy difference is proportional to the free spectral range (FSR) in the cavity. The problem is that FSR changes slightly with the wavelength and is not constant. Hence, to have comb generation over a wide wavelength span, the dispersion needs to be satisfied such that FSR remains constant. This anomalous dispersion was observed intrinsically in different materials [32, 33, 34]. However, to have anomalous dispersion at

different wavelengths, waveguide dispersion needs to be manipulated to compensate for the normal dispersion of the materials. Waveguide dispersion is determined by the microcavity geometry and can be engineered by changing the wedge angle on a silica microdisk [35], or controlling the thickness of the silica disk [14]. Dispersion engineering in silica microdisks is specifically important at shorter wavelengths, where the material dispersion is strong and needs to be made up for by the waveguide dispersion. Therefore, making ultra-thin silica microdisks with high Q is of great interest. However, there are several challenges in making thin silica microdisks. Firstly, the thin silica microdisks tend to buckle under the residual thermal stress [36], which leaves the microdisk mechanically unstable. This is particularly troublesome for large microdisks, which are required for dense microcomb generation. Secondly, wet etching of silica in the fabrication process can lead to surface roughness at the edges of the disk and thus decrease the Q.

To address these challenges novel techniques and processes have been developed, which are briefly explained in this proposal. Firstly a chemo-mechanical polishing technique was introduced to decrease the surface roughness of the microdisk and boost the quality factor. Q values exceeding 10^8 were observed using this method. Moreover, wavelength-dependant quality factor measurements show the Q is no longer limited by the surface scattering but is limited by water absorption at the surface, especially at longer wavelengths. Secondly, a novel rib shape structure has been proposed to solve the buckling problem. Using this new geometry, microdisks with sub-micron thickness and 1 mm in diameter were made with high Q (exceeding 2×10^7), and without buckling. These microdisks are thin enough to satisfy the anomalous dispersion required for microcomb generation at visible to UV wavelengths [14]. There was no noticeable change in optical Q in DPBS (Dulbecco's Phosphate Buffered Saline), since the absorption of visible light is limited in DPBS. Quality factor above 10^7 was

achieved both in the air and DPBS solution, which can potentially be used for single molecule detection in-vitro.

1.2 Contributions

The author was in charge of fabrication and measurements of the microdisks, and part of the discussions and design of experiment for the whole project. The electromagnetic wave simulations presented were done by of Mr. Saeed Farjollahi and Dr. Tao Lu.

1.3 Outline

The thesis is outlined as follows. First, the physical and analytical description of the concepts important to our research will be presented. This will be followed by fabrication techniques developed for increasing the quality factor and reducing the thickness of the microdisks. Finally, the data we gathered for testing the fabricated devices will be presented. In the following two chapters, a general background on Whispering Gallery Mode (WGM) microcavities is provided. Concepts like optical quality factor (Q), mode volume, and dispersion are discussed in detail. Next, the physical and analytical description of the microcomb is given along with the mathematical equations governing the generation of the combs. Furthermore, steps taken by the author to maximize the Q in microdisks were discussed in Chapter 4, along with a detailed discussion on the chemo-mechanical polishing and fabrication and annealing process performed to achieve ultra-high Q microdisks. Moreover, efforts to engineer the dispersion of the microdisks were discussed to achieve anomalous dispersion at visible wavelengths in Chapter 5. In this chapter, dispersion engineering of the microdisks was investigated through the introduction of a novel rib like disk with a thin outer diameter. The mechanical stability of the new structure was also discussed in detail.

Finally, the rib disk fabricated using the CMP process was used to generate preliminary evidence of microcomb both in the air and in the water. A detailed discussion of the comb generated is included in Chapter 6. Chapter 7 summarizes the thesis and provides future directions.

Chapter 2

Whispering Gallery Mode Microcavities

Microcavities, as discussed earlier are devices, that can confine light inside a medium and enhance the light-matter interaction. Among different kinds of microcavities, whispering gallery mode (WGM) microcavities have increasingly seen new applications and are of great interest in the scientific community [18]. WGM microcavities rely on total internal reflection to confine the light inside the medium. Thus the shape of these cavities is circular. The WGM cavity was first observed at St Paul's Cathedral in 1878, where whispers can be heard across the hall [37]. The phenomenon was explained by Lord Rayleigh in the 1910s using sound wave and their propagation in a circular manner in the cathedral [37, 38]. He explained how sound rays could make up the cord of the circular structure of the cathedral, and bounce off the walls, while their intensity is decreasing inversely to the distance traveled, instead of inverse squared intensity reduction of sound waves from a point source. Hence, the whispers can be heard along the circular wall across the cathedral. Although the St Paul's Cathedral is designed for acoustic wave propagation, the optical WGM microcavities

use the same principle to contain the electromagnetic wave inside. The first optical microcavity was reported in the microdroplet by Ashkin et al [39]. In this research, silicon oil droplets with low vapor pressure were used as a microcavity, and Q as high as 10^6, was achieved. WGM microcavities can be categorized by their geometry into different groups. Each geometry has a different fabrication process and can have unique applications. However, the fundamental physics governing the light propagation inside the cavity is the same in different geometries. In this chapter, different types of WGM microcavities based on their geometry will be introduced then basic terminologies will be discussed in more detail.

2.1 Different Types of WGM Microcavities

Based on their geometry, WGM microcavities can be categorized into different types, as seen in Fig. 2.1. The structural differences in these microcavities lead to different properties and require different fabrication processes.

Microdisks as shown in Fig. 2.1 a) are usually fabricated using a low-loss thin film on a substrate. The disk pattern then can be made with lithography and etching, and the substrate will be undercut to form a pillar and to make an air cladding underneath the disk to decrease the optical loss. In contrast, a microring in Fig. 2.1 b) does not have an air cladding surrounding the microcavity, since there is no pillar to support the structure. Hence, the Q factor for microring is usually lower.

Microtoroid is fabricated the same way as the microdisk. However, a final CO_2 laser reflow, changes the edge shape to a toroid-like shape depicted in Fig. 2.1 c) [40]. Microtoroids usually have higher Q since the reflow process effectively removes the surface roughness at the edges caused in the fabrication process. Q values over 100 million (10^8) were reported using this geometry [40]. Fig. 2.1 d) shows another struc-

ture for WGM microcavity. This microsphere structure can be made by reflowing a fiber tip using a high-power laser. Since the fiber tip is being melted by the laser the surface roughness is also absent in this structure and ultra-high Qs can be achieved using this structure. CaF_2 cylindrical microresonator is shown in Fig. 2.1e. This type of microresonator happens to have the highest reported Q due to the low loss nature of CaF_2. Application-specific geometries also can be introduced like Fig. 2.1f. Here a hollow core microbubble is shown for fluid sensing. The specific design allows the fluid to pass through the cavity for maximum light interaction [5]. Ultimately what determines the geometry of the microcavity are the specific requirements for the application and the limitations of the fabrication.

2.2 Materials for WGM Microcavity Fabrication

Here we briefly explain the materials considered for WGM microcavity fabrication. The material selected for microcavity fabrication should be transparent in the operational window, meaning that it should have limited loss such that the resonance condition can be achieved. Ionic compounds like oxides, nitrides, and fluorides are usually used for that purpose. Silicon compounds are among the widely used materials for microcavity fabrication, because of the low loss nature of silicon oxide and nitride, and also the ease of fabrication due to the maturity of the fabrication processes. SiO_2 can be grown easily with high quality using silicon wafers even at low temperatures (less than 500 C$^\circ$) [41]. Shaping silica glass has also been well-known for centuries if not millennia. Thus, silica is a great candidate for WGM microcavity fabrication and a lot of different geometries are used to fabricate silica WGM microcavities. Si_3N_4 is another silicon compound with huge application in WGM microcavity fabrication. Although Si_3N_4 is transparent in a wide window of wavelengths, growing a high-quality

film with limited defect density is not easy. Nevertheless, Plasma enhanced chemical vapor (PECVD), and low-pressure chemical vapor deposition (LPCVD) deposition techniques can be used to grow Si_3N_4 thin films with satisfactory results [42]. There has been efforts to fabricate WGM microcavities with exotic materials like $LiNbO_3$ as well, but growing high quality $LiNbO_3$ remains a challenge [43].

2.3 Optical Quality Factor (Q)

The optical quality factor is related to the lifetime of the photon in the resonator (τ) [44]. The longer the photon can exist inside the cavity before being lost, the higher the Q will be. In terms of WGM microcavities with sufficient photon lifetime, photons will keep accumulating inside the cavity and boost the intensity inside. In this process each photon at a certain wavelength would constructively interfere with the previous photon still circulating inside the cavity. Hence, the intensity of light inside the cavity will be higher by each round trip. The Q factor can also be expressed in terms of energy loss in the cavity.

$$Q = 2\pi f_0 \times \frac{E_{stored}}{P_{loss}} = \omega_0 \tau \tag{2.1}$$

In this equation, f_0 is the resonance frequency, ω_0 is the angular frequency, the E_{stored} is the stored energy in the cavity, the P_{loss} is the power loss in the cavity, and τ is the photon lifetime inside the cavity. Furthermore the Q can be experimentally measured as $\frac{\lambda_0}{\Delta\lambda}$ or $\frac{f_0}{\Delta f}$, where λ_0 and f_0, are resonance wavelength and frequency respectively, and $\Delta\lambda$ and Δf are the full width at half maximum (FWHM) of the Lorenzian peak of the resonance in the spectrum, as shown in Fig. 2.2. The Q factor depends on both the structure of the cavity and also the material from which the cavity has been made. The most important degrading factor for Q is absorption loss,

which is a wavelength-dependent characteristic behavior of the material. Structural limitations on the Q factor are mostly in the form of surface roughness and radiation loss. Therefore, the intrinsic Q can be calculated as [45]

$$\frac{1}{Q_{int}} = \frac{1}{Q_{abs}} + \frac{1}{Q_{ss}} + \frac{1}{Q_{rad}} \tag{2.2}$$

Here Q_{abs}, Q_{ss}, and Q_{rad} represent the light loss due to absorption, surface scattering, and radiation respectively. Note that overall Q is dependent on the light coupling loss as well. However, by careful coupling of the light into the cavity, the effect of coupling loss would be negligible. Hence, to have high Q or ultra-high Q microcavities, we need to mostly address the absorption loss, surface scattering, and radiation loss.

The material's loss is an intrinsic property of the material and cannot be changed. However, vigorous cleaning can decrease the optical loss originating from the contamination, such as hydrocarbons at the surface of the microcavity. Moreover, moisture absorption can have a negative impact on the Q due to optical absorption from water molecules. This is particularly important at near-infrared wavelengths since shorter wavelengths are not absorbed by water molecules [46].

Surface scattering usually comes from the fabrication process, such as imperfect photolithography, etching, or material growth. Thus, to decrease the loss associated with surface scattering one should refine the fabrication process first. Post-fabrication polishing has also been proposed to decrease the roughness [46, 47, 48].

Rayleigh scattering caused by surface roughness limits the Q factor by the equation below for microdisks [49]

$$Q_{ss} = \frac{\lambda_0^3}{\pi^{5/2} n_0 (\delta n^2)^2 \bar{V}^2 \Sigma_{\hat{e}} \bar{u}_s(\hat{e}) G(\hat{e})} \tag{2.3}$$

This equation only holds at the limit, where the correlation length (l_c) is much smaller than the wavelength. Here $\bar{V}$ is equal to $\sqrt{Rl_c}h\sigma_r$, R is the disk radius, l_c is correlation length, h is the disk height, and σ_r is the standard deviation of the roughness, δn^2 is the difference in refractive indices square of the two media and n_0 in the refractive index of the microcavity, $\hat{u}_e$ is $\hat{e}$-polarized electric field energy density at the disk edge normalized to unit modal energy, and $G(\hat{e}) = 4/3, 2, 2/3$ is a geometrical radiation factor for $\hat{e} = \hat{r}, \hat{\phi}, \hat{z}$. The equation shows that surface scattering higher impact on the overall Q at shorter wavelengths [49].

The radiation loss dominated Q, (Q_{rad}), is also affected by the structure of the microcavity. In principle, it is determined by the curvature of the circular boundaries of the microcavities [50]. Therefore, having a small structure with tight bends and corners will lead to higher radiative loss in the cavity.

2.4 Mode Volume

One of the important parameters in defining a WGM microcavity is the mode volume. Although most of the electromagnetic field will be concentrated inside the cavity, there is always some leakage to the surrounding medium. This happens to satisfy the continuity of the electromagnetic wave at the interface of two media and is called the evanescent field. So, the mode volume is the physical volume of the optical mode propagating inside the cavity and can be calculated using the following equation [51].

$$V_m = \frac{\int \epsilon(r)|E|^2 dv}{|E_{max}|^2} \tag{2.4}$$

Here V_m is the mode volume, $|E|$ is the electric field strength, and ϵ is the permittivity.

Both cavity geometry and surrounding medium impact the mode volume. In general, smaller cavities tend to confine the light more, and have smaller mode volume, as shown in Fig. 2.4. Moreover, the evanescent field outside small-size cavities will be stronger, so more light will leak out of the cavity. This can be beneficial to sensing applications. The shape of the microcavity can also change the mode volume as the geometrical confinement of the structure can reduce the mode volume. Thus, a microsphere would have a larger mode volume than a microdisk, or a microtoroid with the same diameter, since there is less vertical confinement in the mircosphere. Furthermore, the difference between the refractive indices of the cavity and the surrounding medium can change the mode volume. For example, a bigger refractive index difference between the two media leads to more confinement of light inside the cavity, and a weaker evanescent field.

2.5 Measurement Setup

Measuring any WGM microcavity would involve designing an apparatus to couple the light in and out of the cavity. One of the easiest ways to couple light into a cavity is free space coupling based on Lorenz-Mie theory [52]. In this case, the free space propagating beam will be directed towards a cavity, some of the light would start circulating inside, but much of it would be scattered. The scattered light then can be analyzed to see the behavior of the cavity. The largest limitation of this method is the limitation to efficiently couple the light in large cavities [52]. The other way

to couple light into a cavity is to take advantage of evanescent field coupling [52]. Evanescent field coupling itself can be sub-categorized based on the components used in tapered fiber coupling [53, 54], prism coupling [55, 56], waveguide coupling [57, 58] and fiber tip couling [59]. Here we use a tapered fiber coupling scheme to couple the light in and out of the cavity.

As can be seen in Fig. 2.5 the fiber would be placed in a holder before making contact with the cavity, in this case, a microsphere. However, before moving the fiber to the setup, the fiber needs to be pulled to reduce its thickness. To do that, we use a hydrogen torch to heat the middle section of the fiber, while gradually pulling it using motors. The placement of the torch and pulling speed need to be adjusted for the lowest loss and thinnest fiber possible. This way we make sure of the mode matching condition between the fiber and the cavity. As can be seen in Fig. 2.6, an interferometer is used as a reference signal to measure the FWHM of the resonance peak more accurately. The sinusoidal signal from the Mach-Zender interferometer will act as a reference by which we can measure the width of the resonance peak. The portion of the light that goes through the cavity will be collected with photodetectors, which are in turn connected to an oscilloscope. We also have a function generator connected to the laser to scan the wavelength of the laser around the resonance wavelength. PCs are added to the system for maximum coupling and to adjust the polarization accordingly. Fig. 2.7 shows the actual measurement setup we use on the optical table.

The way the Mach-Zender interferometer works can be explained using the superposition of two beams interfering with each other. A Mach-Zender interferometer consists of two separate arms one longer than the other. The light entering the interferometer would get separated equally into one of the two branches, and since there is a difference in length in the two arms, there is a phase change ($\Delta\phi$) between the

light propagating in two arms. The intensity of light in the output can be calculated as $\left|E_1 \pm e^{i\Delta\phi}E_2\right|$, where E_1 is the field in branch 1, and E_2 is the field in branch 2. By changing the wavelength one can easily change the $\Delta\phi$ which means the interference of the light at the output can be changed from destructive to constructive. The output signal will be sinusoidal as a function of $\Delta\phi$.

2.6 Dispersion

In optics, dispersion is the change of the phase velocity and associated refractive index with frequency [60]. This is one of the most fundamental features of a wave, and one that is essential for comb generation. The dispersion can be explained as a deviation from the resonance frequencies of the longitudinal modes, with contribution from both the material and the geometry of the structure [10]. The material dispersion is an intrinsic feature of a material and is difficult to alter. However, structure geometrical dispersion or waveguide dispersion can be tuned. Dispersion in microcavities is usually expressed in terms of Free Spectral Range (FSR). If the $\frac{d\Delta\lambda_{FSR}}{d\lambda} > 0$ the dispersion is called "normal dispersion", and if $\frac{\Delta\lambda_{FSR}}{d\lambda} < 0$ the dispersion is called anomalous. Note that these notations might be used interchangeably in other scientific communities. The deviation from the FSR can be explained further using Taylor's expansion below:

$$\omega_\mu = \omega_0 + D_1\mu + \frac{1}{2}D_2\mu^2 + \frac{1}{6}D_3\mu^3 + \frac{1}{24}D_4\mu^4 + ... \tag{2.5}$$

Which can be re-written as:

$$\omega_\mu = \omega_0 + D_1\mu + D_{int} \tag{2.6}$$

Here the μ is the mode index around the center mode $\mu = 0$ [10], $D_1\mu$ is the FSR

(without the effect of dispersion), and the integrated dispersion (D_{int}) is the deviation from the FSR caused by the dispersion. In equation 2.5, D_2 is the dominant term and third and fourth orders are negligible [10]. Using this notation one can find approximate values for dispersion around the center wavelength easily and determine whether the dispersion is anomalous or not. One can show that for the dispersion to be anomalous, D_{int} has to be positive. We know for the dispersion to be anomalous, $\frac{\Delta\lambda_{FSR}}{d\lambda} < 0$ this means $\frac{\Delta\lambda_{FSR}}{d\mu} > 0$ for anomalous dispersion, since $\mu\lambda$ remains constant in a WGM microcavity. By using Eq. (2.5), we have

$$FSR = \omega_\mu - \omega_{\mu-1} = D_1 + \frac{1}{2}D_2(\mu^2 - (\mu-1)^2) \tag{2.7}$$

$$FSR = D_1 + D_2\mu + \frac{1}{2}D_2 \tag{2.8}$$

Now ttaking the rivative of the FSR with respect to μ we get :

$$\frac{\Delta\lambda_{FSR}}{d\mu} = D_2 \tag{2.9}$$

So D_2 has to be positive for anomalous dispersion, and we can infer from equation 2.6 that D_{int} should also be positive. Dispersion can also be expressed in terms of β_2, group velocity dispersion (GVD).

$$\beta_2 = \frac{1}{c}\frac{dn_g}{d\omega} \tag{2.10}$$

Dispersion relation to β_2 can be shown as:

$$\frac{\Delta\lambda_{FSR}}{d\mu} = \frac{\Delta\lambda_{FSR}}{d\omega} \times \frac{d\omega}{d\mu} \tag{2.11}$$

where:

$$FSR = \frac{2\pi c}{n_g L} \tag{2.12}$$

and:

$$n_g L = \mu\lambda \tag{2.13}$$

$$\frac{\Delta\lambda_{FSR}}{d\omega} = -\frac{2\pi c}{n_g^2 L}\frac{dn_g}{d\omega} \tag{2.14}$$

$$\frac{d\omega}{d\mu} = \frac{2\pi c}{n_g L} \tag{2.15}$$

From Eq 2.11,2.14, and 2.15 we can see:

$$\frac{\Delta\lambda_{FSR}}{d\mu} = \frac{-4\pi^2 c^3}{n_g^3 L^2}\beta_2 \tag{2.16}$$

and

$$D_1 = \frac{2\pi c}{n_g L} \tag{2.17}$$

using Eq 2.9 we can conclude:

$$D_2 = -\frac{c}{n_g} D_1^2 \beta_2 \tag{2.18}$$

Hence, for anomalous dispersion β_2 should be negative as can be seen in Fig. 2.9. Using GVD, one can calculate D_{int} and vice versa. Both GVD and D_{int} can be simulated by finding the resonance frequencies around a center (pump) frequency (ω_0), and a polynomial fit to represent $\omega - \mu$ data. In most cases, a second-order polynomial would provide a satisfactory fitting, since D_3, D_4, and higher orders are negligible compared to D_2. However, in rare occasions, a third order should be added

to represent D_3 [14]. The following graphs shows simulated values for GVD and D_{int} in different wavelength windows.

[h] Fig. 2.9, shows simulated values for D_{int} and β_2 for a rib disk structure around 1550 nm wavelength. The positive D_{int}, and negative values for β_2 show the anomalous dispersion of the medium in the wavelength range specified. The parabolic shape of the D_{int} curve, represents the dominant D_2 term, and the concave shape confirms the positive value of D_2.

2.7 Geometrical Considerations of Dispersion

As mentioned before, the geometry of a microcavity can also affect the dispersion through what is called waveguide dispersion. Since the geometry of a WGM microcavity can be tuned during the fabrication process, most of the effort to engineer a desired dispersion has been invested in changing the shape of the cavity. Whether it is tuning of the thickness [14, 9], or the wedge angle [61], shape tuning has been used to effectively move the dispersion from normal to the anomalous regime. Here we mostly describe the effect of wedge angle, size, and thickness on the dispersion.

As can be seen in Fig. 2.10, the zero dispersion will move to shorter wavelengths by increasing the wedge angle. That basically means the anomalous dispersion regime will be extended to shorter wavelengths. The reason for this can be attributed to the fact that tighter wedge angles tend to push the modes further into the cavity, hence reducing the effective radius of the cavity. This in turn will increase the FSR of the mode family. This increase in FSR in longer wavelengths contributes to overall normal dispersion in the cavity [10]. The effect of the wedge in changing the effective radius will be a lot lower at larger wedge angles. The other geometrical aspect with a huge effect on the dispersion to be considered is the thickness. As a general

rule decreasing the thickness of a silica microdisk (or microtoroid) will contribute to anomalous dispersion. This can be explained by mode compression or confinement in thinner microcavities [10].

As can be seen in Fig. 2.11, the dispersion moves to the anomalous regime with decreasing thickness. So as can be seen the geometry of a microcavity can greatly impact the dispersion. Hence, engineering geometry can give us a powerful tool to alter the dispersion to our liking. Dispersion can also be an intrinsic property of a medium. In the next section, the material dispersion will be explained in more detail.

2.8 Material Dispersion

The material dispersion is an intrinsic property of a material, and it mostly depends on how the atoms inside the material react to electromagnetic waves. for most materials (including silica) the shorter visible wavelength means higher interaction with the atoms since the frequency of the wave is closer to the resonance frequency of the atoms. Hence the refractive index increases at shorter wavelengths [62, 63].

As can be seen in Fig. 2.12, the increase of refractive index in shorter wavelength gives rise to negative D, which means the dispersion moves to the anomalous regime. As mentioned before, the change of the refractive index by wavelength depends on the atomic response of the material to electromagnetic waves. The closer the wavelength is to the resonance frequency of the atoms, the more powerful the response of the medium would be to the wave. Therefore the refractive index will increase.

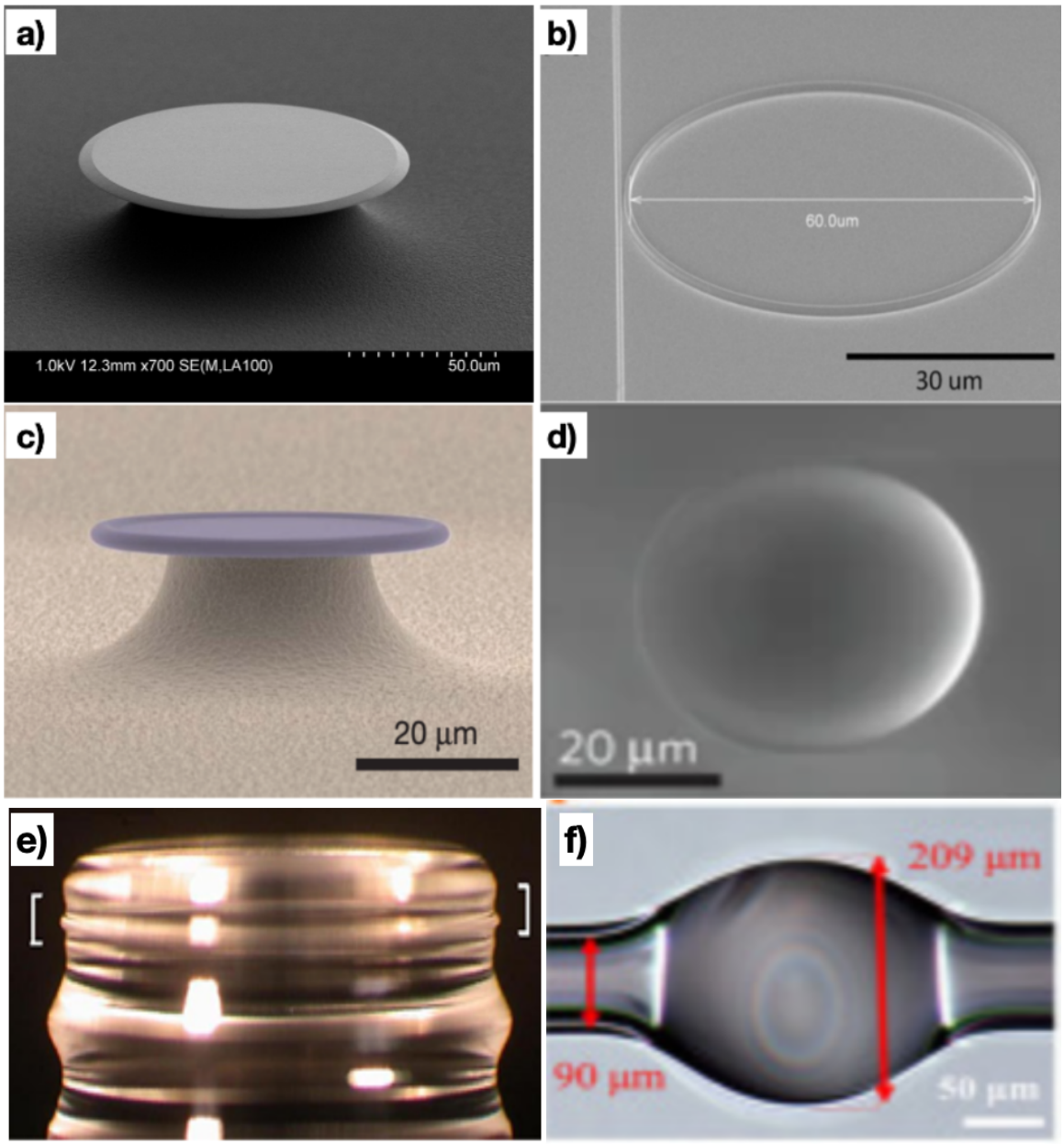

Figure 2.1: a) Microdisk, b) Microring [1], c) Microtoroid [2], d) Microsphere [3], e) Cylindrical microresonator [4], and f) Microbubble resonator [5]

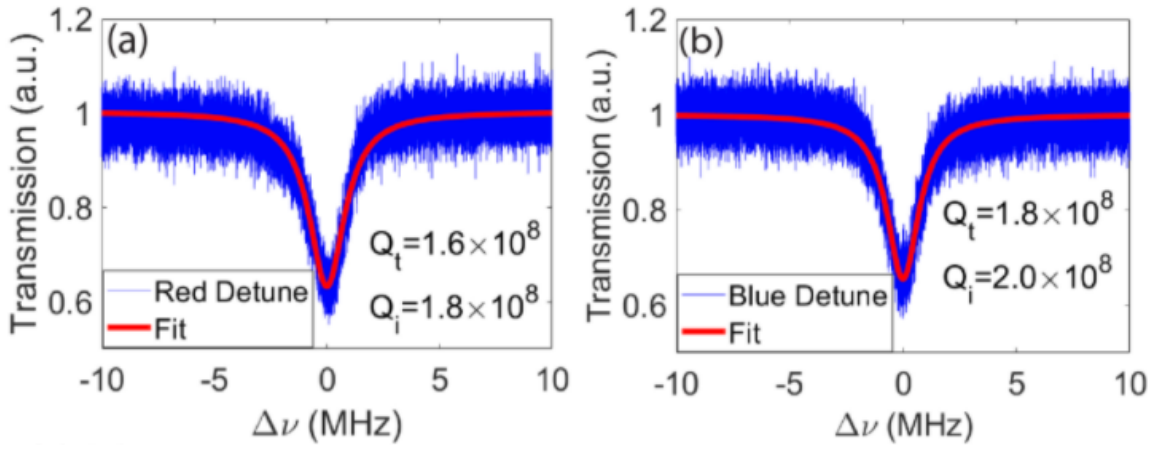

Figure 2.2: Q measurements for red detuned a), and blue-detuned b) scan with the associated Lorezian fit. The slight difference between the total Q (Q_t), and the intrinsic Q (Q_i) is because of the coupling loss

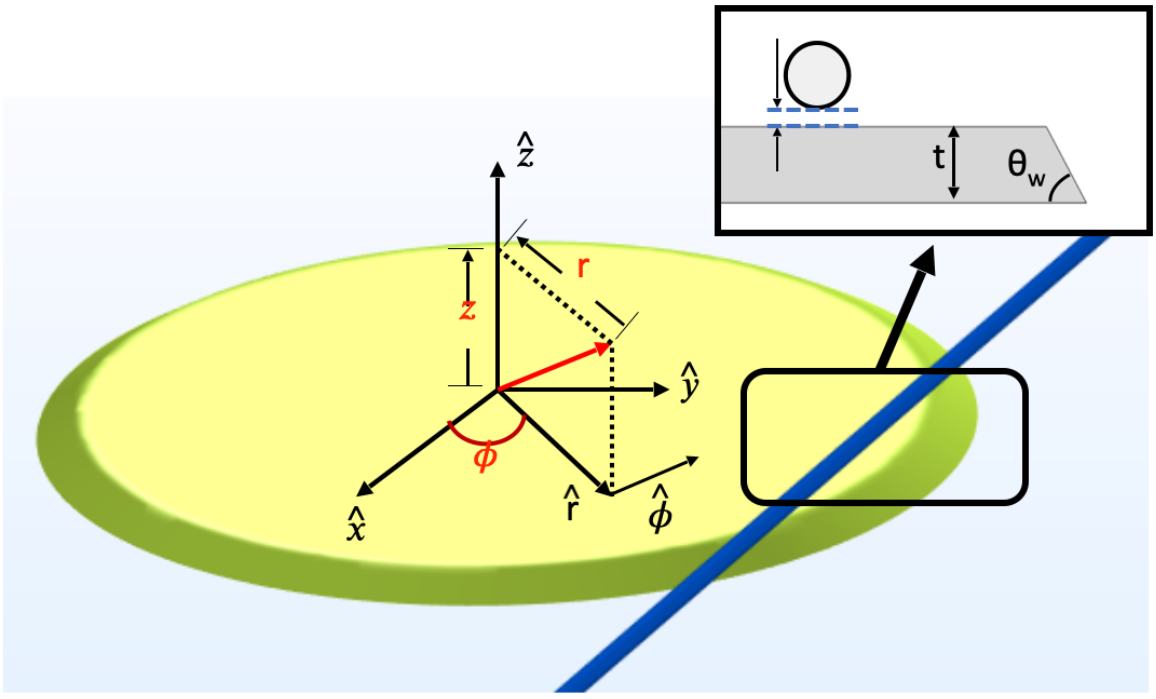

Figure 2.3: Cylindrical coordinates of a disk with the tapred fiber on top [6]

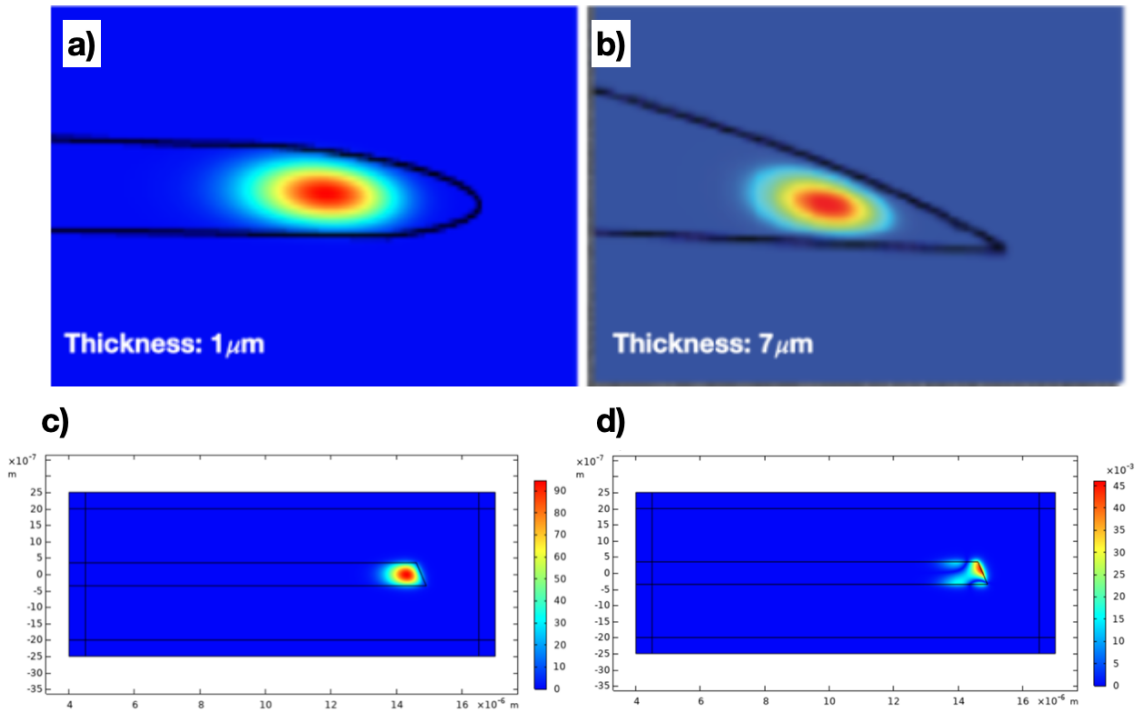

Figure 2.4: a) and b), intensity of the TE polarized WGM mode in microdisks with different thickness, c) E_r and d) H_r fields distribution for $LiNbO_3$ microdisks.

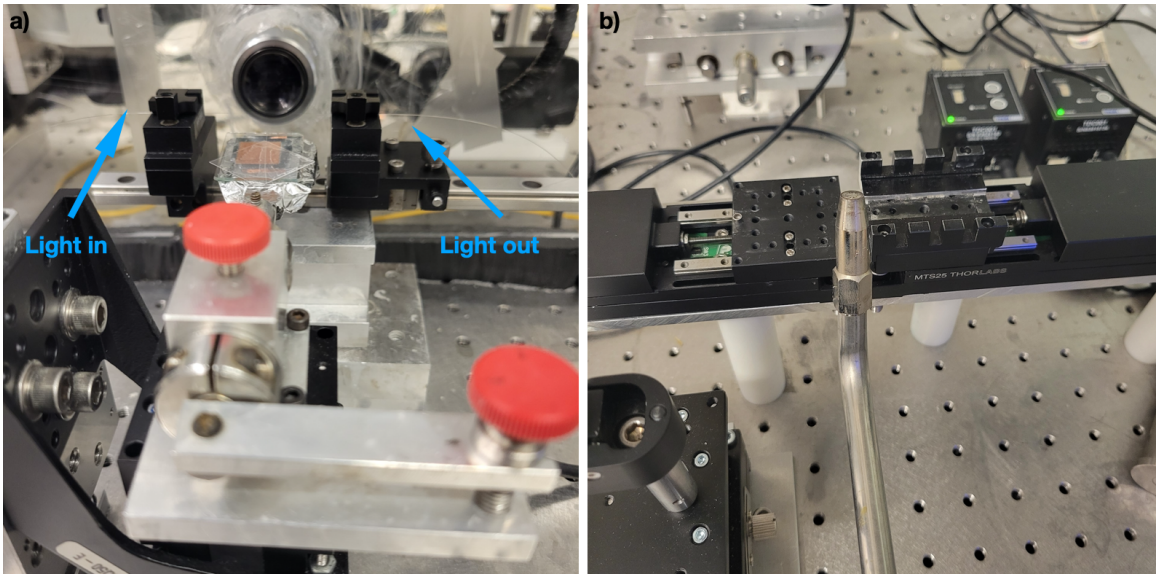

Figure 2.5: The light coupling apparatus for our microdisks, a)fiber holder on the stage b) the torch used for fiber pulling

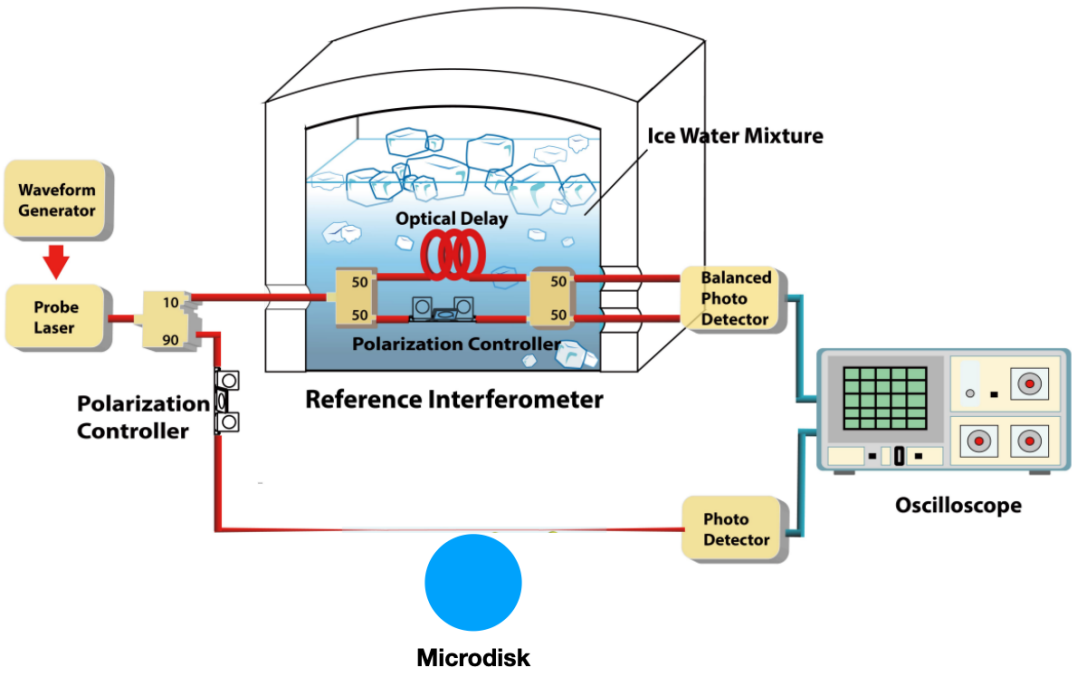

Figure 2.6: The schematic of a Q measuring setup. The ice water would be added to minimize the temperature fluctuation's effect on the interferometer, the polarization controllers enable us to achieve maximum coupling [7]

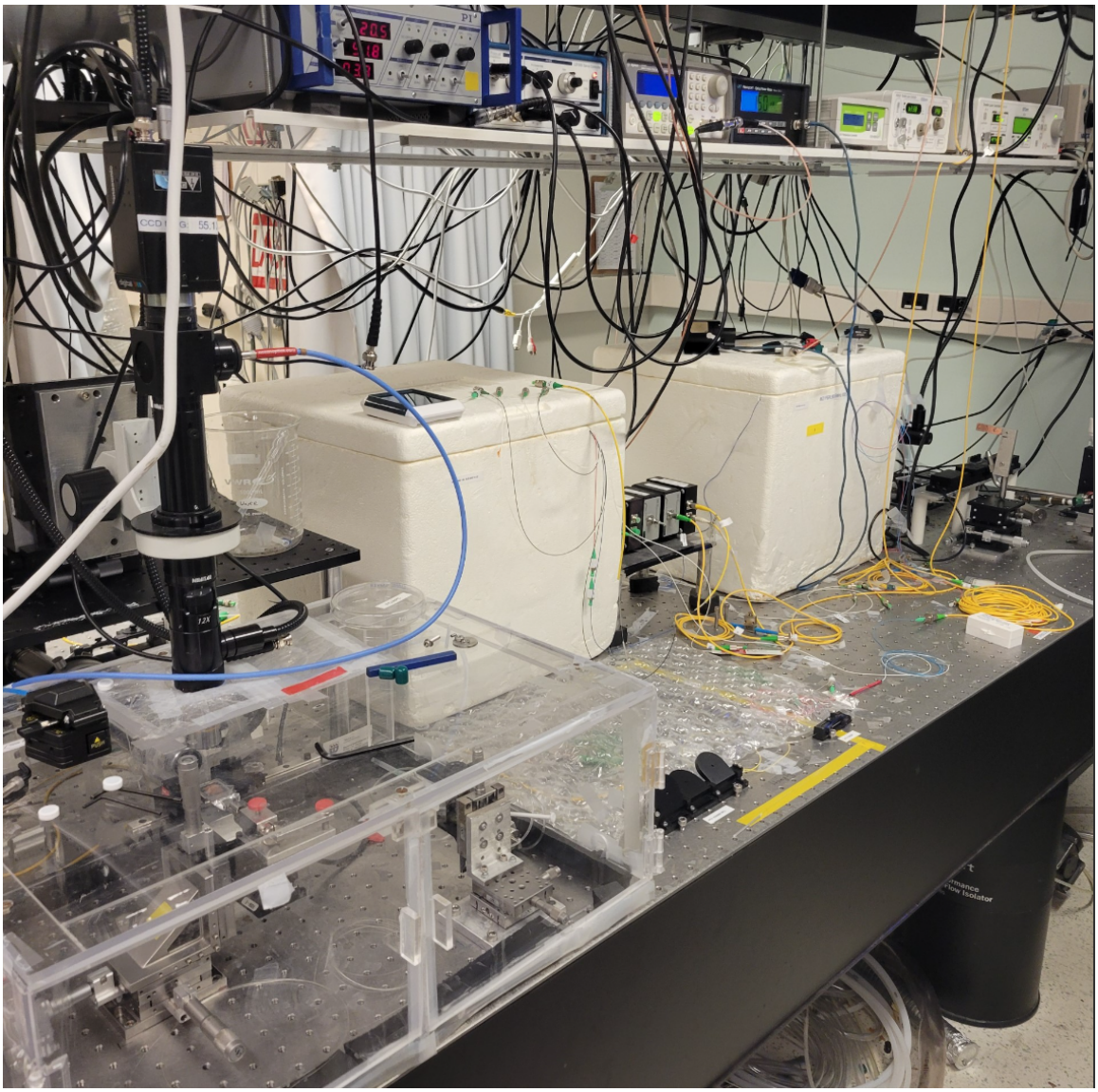

Figure 2.7: Optical measurement setup

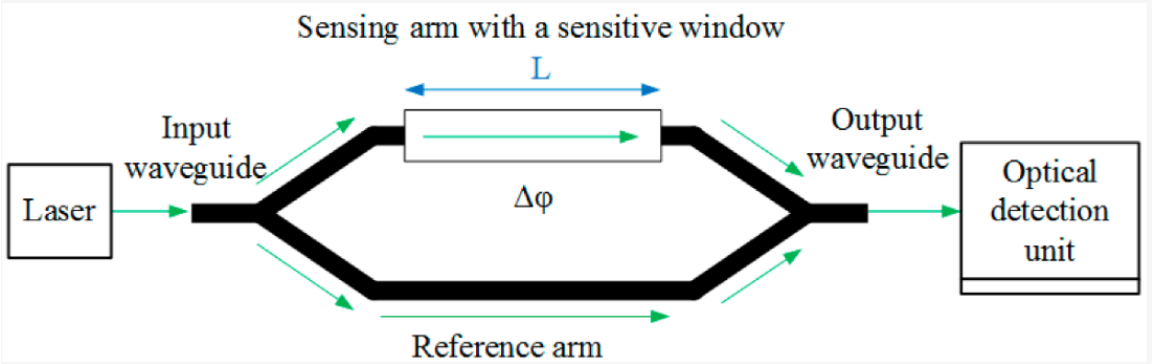

Figure 2.8: Mach-Zender interferometer schematic [8]

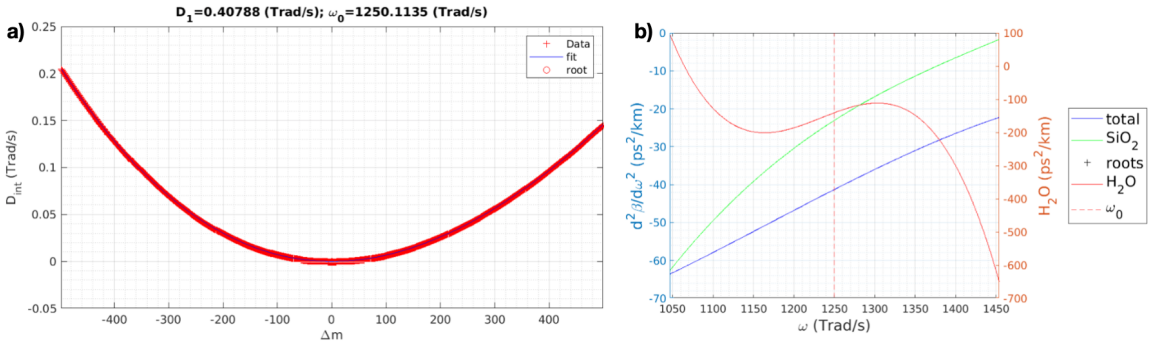

Figure 2.9: Simulated D_{int} and β_2 in 1300 nm- 1800 nm range for the fundamental TE mode of the 1mm rib disk in [9]. The D_{int} is shown in a) as a function of azimuthal mode number away from the center wavelength of 1550 nm, and b) is the associated β_2 for the same wavelength window. β_2 of water is included in b) as a reference to a different medium

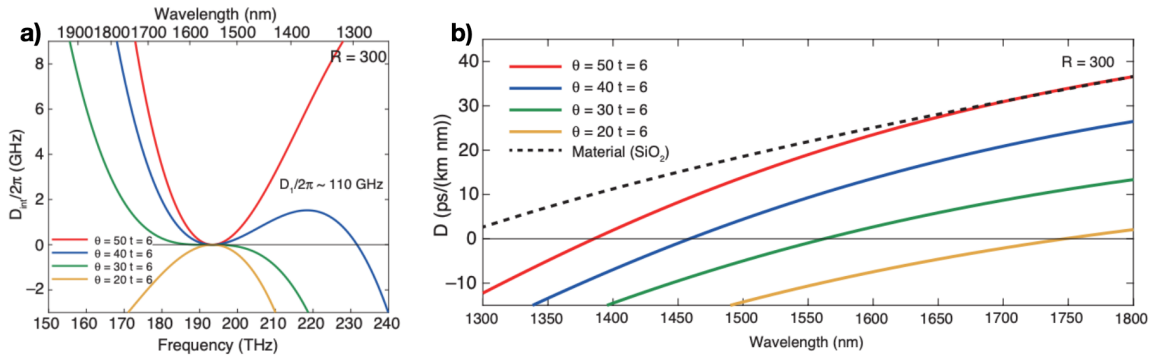

Figure 2.10: The simulated D_{int}(a) and D(b) vs frequency and wavelength of a microdisk with 6 μm thickness and 300 μm of radius [10]. Copyright, 2020 De Gruyter

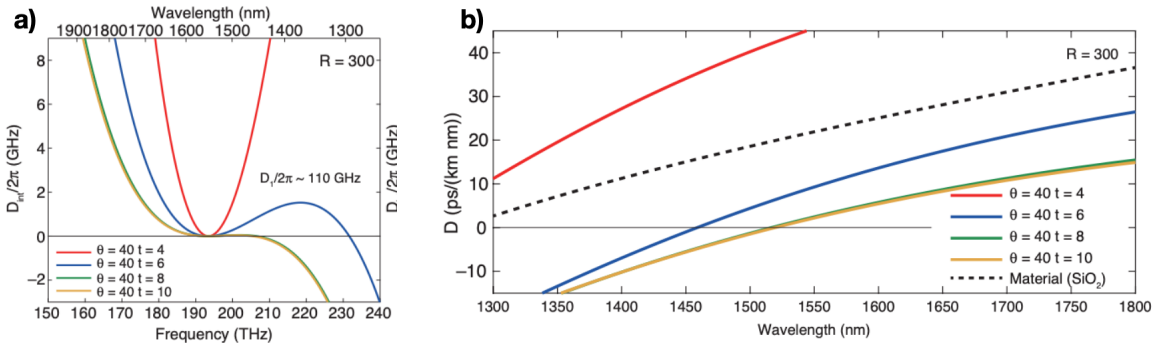

Figure 2.11: The simulated D_{int}(a) and D(b) vs frequency and wavelength of a microdisk with a fixed wedge angle and 300 μm of radius [10]. Copyright, 2020 De Gruyter

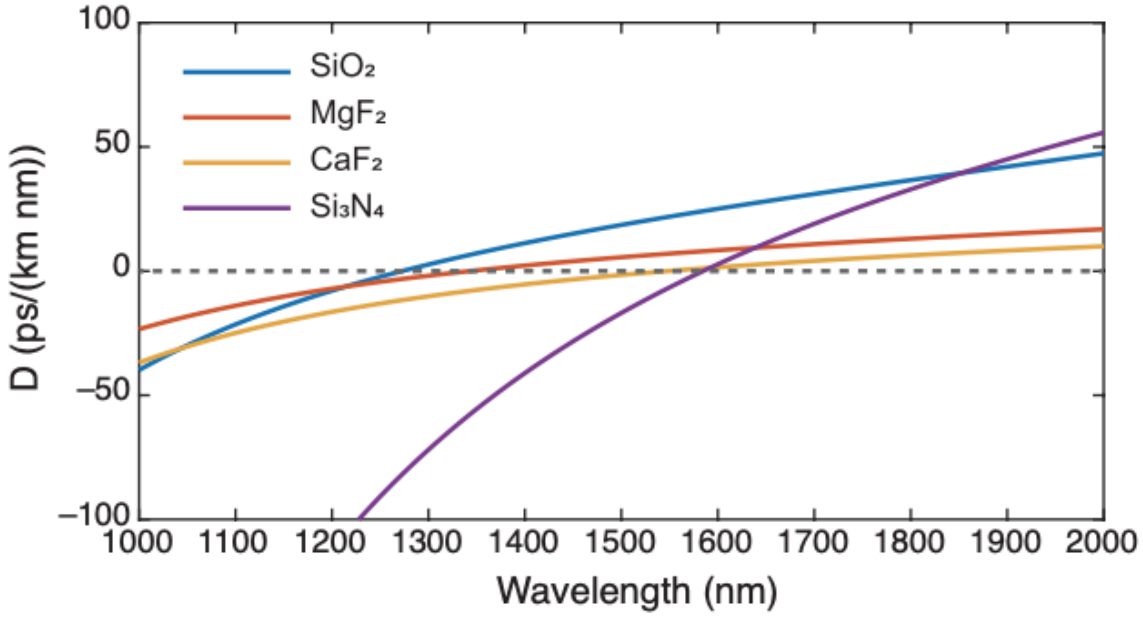

Figure 2.12: Dispersion for four different materials vs wavelength [10]. Copyright 2022, De Gruyter

Chapter 3

Microcomb Generation

Recent advances in frequency microcomb, have opened the door for new applications ranging from timekeeping and exoplanet hunting to spectroscopy and sensing [11, 64, 29]. Microcomb as discussed earlier, are a series of equally distant peaks in the spectrum which are normally produced using the nonlinear response of the material to the electromagnetic wave.

Two of the most common ways of generating broad spectra of microcomb are supercontinuum generation (SCG) in optical waveguides, and Kerr-comb generation (KCG) [11]. In the SCG process, ultra-short pulses from a mode-locked laser would pass through a waveguide. The light then goes through a third-order ($\chi^{(3)}$) nonlinear process known as parametric four-wave mixing (FWM). This process effectively extends the spectrum with the spacing, which is determined by the pulse repetition Fig. 3.1(left). On the other hand, KCG process generates comb using a continuous wave (CW) laser and a passive microresonator. This process also required FWM nonlinear response in the microresonator, but the repetition rate is determined by the free spectral range (FSR) of the cavity Fig. 3.1(right). Note that both processes required desirable dispersion and strong light-matter interaction for the nonlinear

FWM process to happen [11].

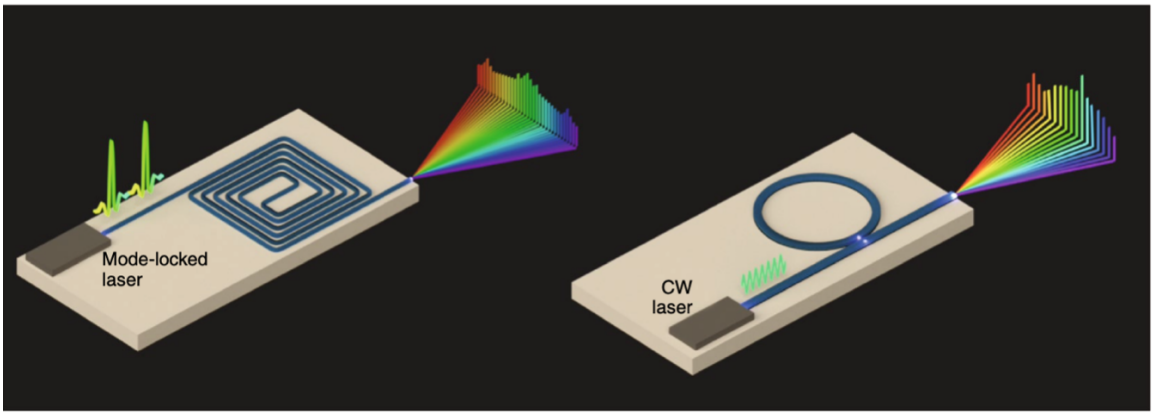

Figure 3.1: Left: SCG of microcomb using a dispersion-engineered waveguide and a mode-locked laser, ultra-short pulses would expand in the spectrum upon passing through the waveguide, with spacing determined by the repetition rate. Right: KCG of microcomb using a CW laser and a dispersion-engineered microresonator, with spacing determined by the FSR of the microresonator [11]. Copyright, 2019 Nature Publishing Group

3.1 Soliton Microcombs

The word "Soliton", was introduced to refer to localized solutions of integrable nonlinear systems [65]. Dissipative solitons is a term introduced to describe solitory waves in nonlinear optical systems with nonlinear loss or gain [65]. So, dissipative optical solitons are wave packets of light confined in a nonlinear medium, which are stable because of the energy balance [65]. Therefore the main difference between the dissipative soliton and conventional soliton is the loss-gain balance of energy, which is essential to the stability of the dissipative soliton.

Dissipative solitons can form inside a nonlinear cavity pumping with a CW laser. Solitons in this case basically rely on a balance between dispersion and Kerr-third order nonlinearity on one hand, and cavity loss and parametric frequency conversion of the pump light on the other [12]. The result is a wave packet of light, which retains

its shape when propagating inside the WGM cavity. Moreover, an optical system can have more than one soliton formed inside the cavity, which results in a much denser comb [12].

The basic requirements for temporal dissipative soliton formation can be summed up in two conditions: Kerr nonlinearity, and anomalous dispersion [12]. Meeting both these requirements means the energy and momentum conservation for the FWM process(Fig.3.2 b) to happen is satisfied. So, finding nonlinear materials with high enough $\chi^{(3)}$, and anomalous dispersion is essential to make microcavities capable of generation microcomb. Fig 3.2(b), shows how the FWM process can happen in a medium to help generate the comb.

Generating of a soliton microcomb requires a fine balance between nonlinearity, in this case, Kerr nonlinearily, and dispersion on one hand, and loss and gain in the cavity on the other. Soliton existence can be shown on an osciloscope (OSC) signal as a step in the spectrum [13]. These steps can be described by analyzing the bistability curve in a cavity.

Fig 3.3 shows how the intracavity power of a resonator changes with laser detuning in the presence of a nonlinearity. It is important to understand that the region in the curve shown with a dashed line is unstable and therefore, impossible to achieve. Thus, in reality, there is an abrupt drop from the blue detuned region to the red, with a sharp decrease in power. [12] Further understanding the comb generation requires more analyzing of the bistability curve.

As shown in Fig. 3.4, the soliton formation happens in the form of steps in between bistability curves. The soliton pulse formed would have a bigger phase shift and would be moving along the upper (blue detuned) branch of another bistability curve [13]. The size of the step depends on the fraction of the light propagating with the soliton pulse compared to the whole power coupled, which itself depends on the high peak

power of the soliton [13].

3.2 Visible Wavelength Comb Generation

As discussed in the previous chapter, both anomalous dispersion and Kerr nonlinearity are needed for comb generation. Kerr nonlinearity is an intrinsic property of the material and is normally seen in materials with inversion symmetry like silca [2]. That makes silica one of the candidates for comb generation. Although, comb generation has successfully been demonstrated for other materials, [66, 67, 68] unique properties of silica, like the ease of fabrication, and very low optical loss, make it more interesting than many other exotic materials for comb generation.

Despite recent advances in silica microcavities, challenges remain for on-chip silica-based microcomb generation. The biggest challenge is the dispersion, especially for short wavelengths. Although soliton microcomb has been demonstrated before [14], comb generation in the visible range has not been possible so far. The reason is the normal dispersion relation of silica ($\frac{dn}{d\lambda} < 0$) in short wavelengths, which makes comb generation impossible without dispersion engineering, since the anomalous dispersion($\frac{dn}{d\lambda} > 0$) is needed for comb generation.

Efforts have been invested in dispersion engineering of silica microdisks by geometry manipulations, such as altering the wedge angle or disk thickness [14, 35]. However, dispersion engineering at the visible range is still hard to achieve. Although disk thickness reduction seems promising for short wavelength comb generation using silica microdisks [14] (see Fig.3.5), the mechanical instability, and buckling severely reduce the applications of this method. This buckling comes from the stress built up caused by the difference between silicon and silica thermal expansion coefficients [36].

The curves in Fig. 3.5 show the calculated dispersion of two hybridized families.

TE2 and TM1 modes are degenerate at certain thicknesses, therefore they can hybridize to form a mode family and lift the degeneracy [14]. For the degeneracy to be lifted, the reflection symmetry needs to be broken [69]. This can happen by the wedge angle at the edge of the microdisk. The lifted degeneracy produces one normally dispersed mode and one with strong anomalous dispersion, which is required for microcomb generation. This mode hybridization is greatly dependent on the thickness. So, by decreasing the thickness anomalous dispersion can be achieved at shorter wavelengths. Controlling the thickness is not the only way to generate visible comb in microcavities. Choi, et al, for instance [15], use local anomalous dispersion happening at the visible to IR range due to avoided mode crossing (AMX) on microtoroid structures to generate comb in water.

As can be seen in Fig 3.6, the eigenfrequencies change dramatically around the mode crossing area and quality factor drops [15]. The response of the system to minimize the effects of the mode crossing causes local anomalous dispersion, which can give rise to the comb generation. The comb lines are few and far between in Fig 3.6, which limits this technique to meaningfully use the microcomb for some applications like sensing. Evidence of AMX has been reported in other works as well [16]. In this work Si_3N_4 microrings were used to generate microcombs in a wide range covering biological windows (less than 1 μ m) [16].

As can be seen in Fig 3.7, a huge change in dispersion can happen due to AMX, which causes the TE00 mode to have anomalous dispersion. The comb generated in [16] also takes advantage of the geometry tuning of the microring for dispersion engineering. Finally, it can be concluded that geometrical considerations like controlling the thickness [14], changing the dimensions [16], or even increasing the wedge angle [61], can be utilized to push anomalous dispersion in the media towards visible wavelengths, which is necessary for microcomb generation. In the following

section mathematical description of solitons will be discussed, using the nonlinear Schrodinger's equation. Most of the analytical descriptions and derivations are written using [53] and [12].

3.3 Analytical Description of Soliton

The first part of this section shows a mathematical description of nonlinear Schrodinger's equation for optical medium based on [70, 71].

Solution for plane waves satisfying the Helmholtz equation should have a Fourier integral form of:

$$\phi(x,t) = \int_{-\infty}^{\infty} F(k) \exp\{i(kx - \omega(k)t)\} dk \tag{3.1}$$

Here the ω value is very close to ω_0 and a Taylor's expansion gives:

$$\omega(k + \delta k) = \omega_0 + (\delta k)\omega_0{}' + (\delta k)^2 \omega_0{}'' + ... \tag{3.2}$$

Substituting 3.2 into 3.1:

$$\phi(x,t) = \psi(x,t) \exp\{i(k_0 x - \omega_0 t\} + c.c \tag{3.3}$$

Where:

$$\psi(x,t) = \int_0^{\infty} F(k_0 + \delta k) \exp\left\{ i(x - \omega' t)\delta k - \frac{1}{2} i\omega''(\delta k)^2 t \right\} d(\delta k) \tag{3.4}$$

Here δk is very small and $\omega(-k) = -\omega(k)$ the amplitude of $\psi(x,t)$ is a slowly varying function of $x^* = (x - \omega' t)$ and t [71] with slow variables ξ and τ.

$$\xi = \epsilon(x - \omega' t), \tau = \epsilon^2 t \tag{3.5}$$

Where ϵ is the dielectric constant, therefore:

$$\phi(x,t) = A(\xi,\tau)\exp\{i(k_0 x - \omega_0 t)\} + c.c \tag{3.6}$$

$$A(\xi,\tau) = \int F(k_0 + \delta k)\exp\left[i\delta k(x - \omega_0' t) - \frac{1}{2}\omega''(\delta k)^2 t\right] d(\delta k) \tag{3.7}$$

$$A(\xi,\tau) = \int F(k_0 + \delta k)\exp\left\{i(\xi - \frac{1}{2}\omega_0''\tau)\right\} d(\epsilon) \tag{3.8}$$

Simple calculation gives:

$$A_\tau = -\frac{1}{2} i\omega_0'' A, A_{\xi\xi} = -A \tag{3.9}$$

Which gives the linear Schrodinger's equation as:

$$iA_\tau + \frac{1}{2}\omega_0'' A_{\xi\xi} = 0 \tag{3.10}$$

In order to include nonlinearity in the system we replace wavenumber k and angular frequency ω with $k - i\frac{\partial}{\partial x}$ and $\omega - i\frac{\partial}{\partial t}$ respectively. In the presence of non linearity we can define dispersion as:

$$D(k - i\frac{\partial}{\partial x}, \omega - i\frac{\partial}{\partial t}, |A|^2)A = 0 \tag{3.11}$$

If we consider small nonlinearity we can assume A is a slowly varying function and D can be expanded as:

$$\begin{aligned} D(k,\omega,0) - i(D_k\frac{\partial}{\partial x} - D_\omega\frac{\partial}{\partial t})A \\ -\frac{1}{2}(D_{kk}\frac{\partial^2}{\partial x^2} - 2D_{k\omega}\frac{\partial^2}{\partial x\partial t} + D_{\omega\omega}\frac{\partial^2}{\partial t^2})A + \frac{\partial D}{\partial |A|^2}|A|^2 A = 0 \end{aligned} \tag{3.12}$$

We then consider two transformation $x^* = x - C_g t$ and $t^* = t$. Assuming $A = O(\epsilon)$, $\frac{\partial}{\partial x^*} = O(\epsilon)$, $\frac{\partial}{\partial t^*} = O(\epsilon^2)$, and retaining all terms up to $O(\epsilon^3)$:

$$i\frac{\partial A}{\partial t} + p\frac{\partial^2 A}{\partial x^2} + q|A|^2 A = 0 \tag{3.13}$$

Here $C_g = -\frac{D_\omega}{D_k}$, $p = \frac{1}{2}(\frac{\mathrm{d}Cg}{\mathrm{d}k})$, and $q = \frac{1}{D_\omega}(\frac{\partial D}{\partial |A|^2})$

Eq 3.13 is the non linear Schrodinger's equation. If the nonlinear dispersion has a form of $\omega = \omega(k, a^2)$ then using Taylor's expansion at $k = k_0$, and $|a|^2 = 0$, ω can be expressed as:

$$\omega = \omega_0 + (k - k_0)\omega' + \frac{1}{2}(k - k_0)^2\omega'' + \frac{\partial \omega}{\partial |a|^2}|a|^2 \tag{3.14}$$

Replacing $\omega - \omega_0$ with $i\frac{\partial}{\partial t}$ and $k - k_0$ with $-i\frac{\partial}{\partial x}$ and assuming $a = a(x, t)$ we get:

$$i(a_t + \omega_0' a_x) + \frac{1}{2}\omega'' a_{xx} + \gamma|a|^2 a = 0 \tag{3.15}$$

Where:

$$\gamma = -(\frac{\partial \omega}{\partial |a|^2}) = constant \tag{3.16}$$

Now if we replace $\xi = x - \omega_0' t$ and $\tau = t$ the term a_x will drop out of 3.15 and we will have:

$$ia_\tau + \frac{1}{2}\omega_0'' a_{\xi\xi} + \gamma|a|^2 a = 0 \tag{3.17}$$

which is the normalized nonlinear Schrodinger's equation.

The following section is based on the work shown in the supplementary material at in [12]. Here we start with non-linear Schrodinger's equation to mathematically predict the behavior of the soliton formation in a nonlinear medium.

$$i\frac{\partial \Psi}{\partial t} + \frac{1}{2}\alpha\frac{\partial^2 \Psi}{\partial \phi^2} + \gamma\left|\Psi^2\right|\Psi = 0 \tag{3.18}$$

This is the dimensionless form of the nonlinear Schrodinger's equation. Here α is a dispersion-related constant and γ is related to nonlinearity in the medium [71]. It can be concluded from the equation 3.18, that if the $\alpha\gamma < 0$ the equation has solutions in the form of bright or breather solitons [71].

Describing the internal field in a soliton, using the nonlinear Schrodinger's equation as in [72]:

$$\frac{\partial A}{\partial t} - i\frac{1}{2}D_2\frac{\partial^2 A}{\partial \phi^2} - ig|A|^2 A = -(\frac{\kappa}{2} + i(\omega_\mu - \omega_p))A \tag{3.19}$$

Here we have:

$$A(\phi, t) = \Sigma_\mu A_\mu e^{i\mu\phi - i(\omega_\mu - \omega_p - \mu D_1)t} \tag{3.20}$$

As can be seen the ϕ value is dispersion dependant here and A is the slowly varying amplitude [12, 71]. Here g can be calculated by $g = \frac{\hbar\omega^2 c n_2}{{n_0}^2 V_{eff}}$, where n_2 is the nonlinear refractive index and V_{eff} is the effective mode volume. Trying to rewrite 3.19 in the dimensionless form of 3.18 we get:

$$i\frac{\partial \Psi}{\partial \tau} + \frac{1}{2}\frac{\partial^2 \Psi}{\partial \theta^2} + |\Psi|^2\Psi = (-i + \xi_0)\Psi + if \tag{3.21}$$

Here $f = \sqrt{\frac{8g\eta P_{in}}{\kappa^2\hbar\omega_0}}$, and $\tau = \frac{\kappa t}{2}$, where κ is the decay rate in the cavity, η is the coupling factor and $\xi_\mu = \frac{2(\omega_\mu - \omega_0 - D_1\mu)}{\kappa}$ is a representation of detuning. In order to have dimensionless values, $\theta = \phi\sqrt{\frac{\kappa}{2D_2}}$, $\Psi(\tau, \theta) = \Sigma a_\mu e^{i\mu\phi}$
Solving 3.21 at steady state ($\frac{\partial \Psi}{\partial \tau} = 0$) we get:

$$\Psi = \Psi_0 + Be^{i\Phi_0} sech(B\theta) \tag{3.22}$$

The solution is valid at $\xi_0 >> 1$, which means the decay rate is very small. Solving

for Ψ_0 :

$$(|\Psi_0|^2 - \xi_0 + i)\Psi_0 = if \tag{3.23}$$

$$\Psi_0 = \frac{if}{(|\Psi_0|^2 - \xi_0 + i)} \approx \frac{f}{\xi_0^2} - i\frac{f}{\xi_0} \tag{3.24}$$

$$\begin{aligned} B &\approx \sqrt{2\xi_0} \\ cos(\phi_0) &= \frac{\sqrt{8\xi_0}}{\pi f} \end{aligned} \tag{3.25}$$

expanding 3.22 for more than one soliton we get:

$$\Psi(\phi) = \Psi_0 + \left(\frac{4\xi_0}{\pi f} + i\sqrt{2\xi_0 - \frac{16\xi_0^2}{\pi^2 f^2}}\right) \sum_{j=1} N sech(\sqrt{\frac{\xi_0}{d2}}(\phi - \phi_j) \tag{3.26}$$

We can use the Fourier transformation of the $\Psi(\phi)$ to obtain the optical spectrum of a soliton. Note that the Fourier transform of a hyperbolic secant function would be a hyperbolic secant function as well.

$$\Psi(\mu) = F.T\left(\sqrt{2\xi_0} sech(\sqrt{\frac{\xi_0}{d_2}}\phi)\right) = \sqrt{\frac{d_2}{2}} sech\left(\frac{\pi\mu}{2}\sqrt{\frac{d_2}{\xi_0}}\right) \tag{3.27}$$

Using $\omega = \omega_p + \mu D_1$ we get:

$$\begin{aligned} \Psi(\omega - \omega_p) &= \sqrt{\frac{d_2}{2}} sech\left(\frac{\omega - \omega_p}{\Delta\omega}\right) \\ \Delta\omega &= \frac{2D_1}{\pi}\sqrt{\frac{\xi_0}{d_2}} \end{aligned} \tag{3.28}$$

We can also conclude:

$$\Psi(t) = \sqrt{2\xi_0} sech\left(\frac{t}{\Delta t}\right)$$
$$\Delta t = \frac{1}{D_1}\sqrt{\frac{d_2}{\xi_0}} \tag{3.29}$$

It means that the width of a soliton is directly proportional to the detuning constant and inversely proportional to decay rate κ. in the following chapters, the author's contributions will be discussed in detail. Firstly, fabrication processes to increase quality factors will be discussed, then a novel rib disk geometry will be introduced to engineer the dispersion for comb generation. Finally results for comb generation in air and water will be presented at around 780 nm wavelength.

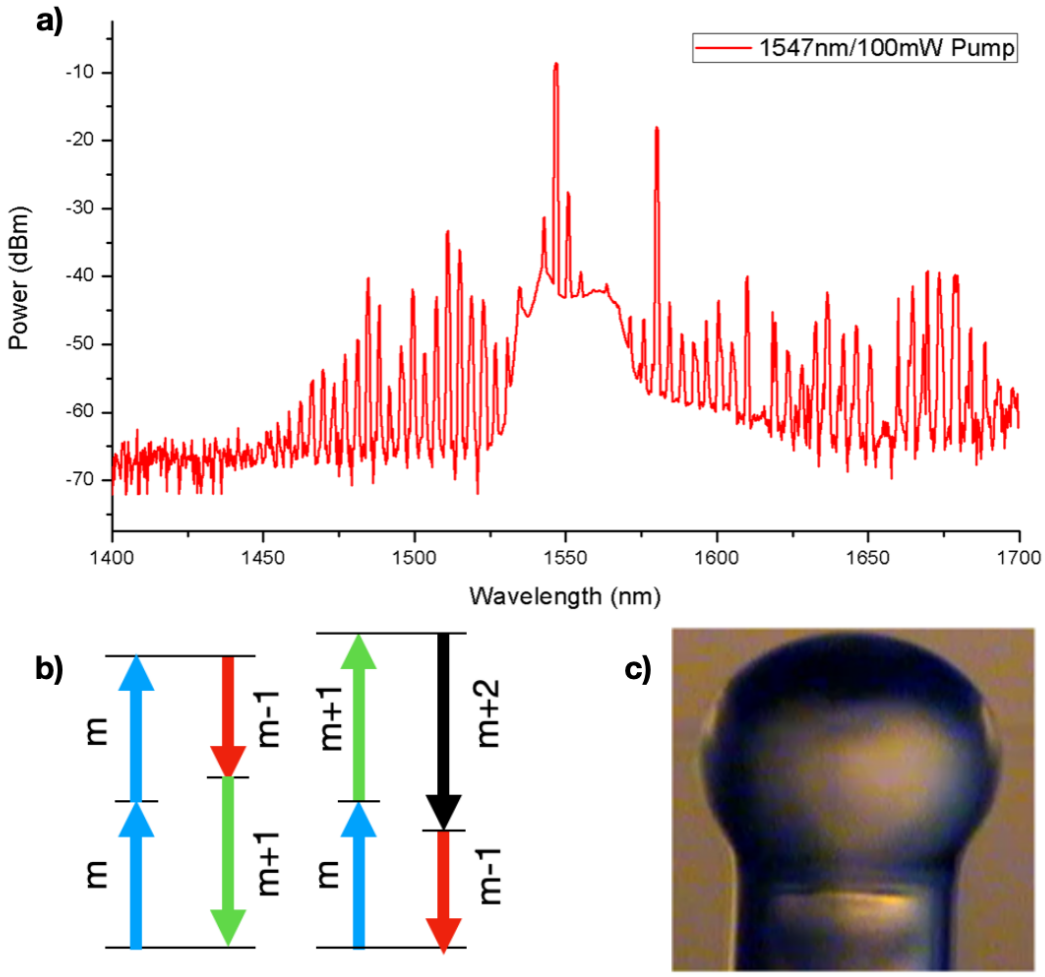

Figure 3.2: a) Spectrum of parametric frequency conversion observed in a microsphere pumped at 1550 nm, units of dBm represents a logarithmic power relative to power of 1mW, b) Schematic of a degenerate (left) and non-degenerate (right) FWM among cavity eigenmodes, c) SEM image of a silica microsphere.

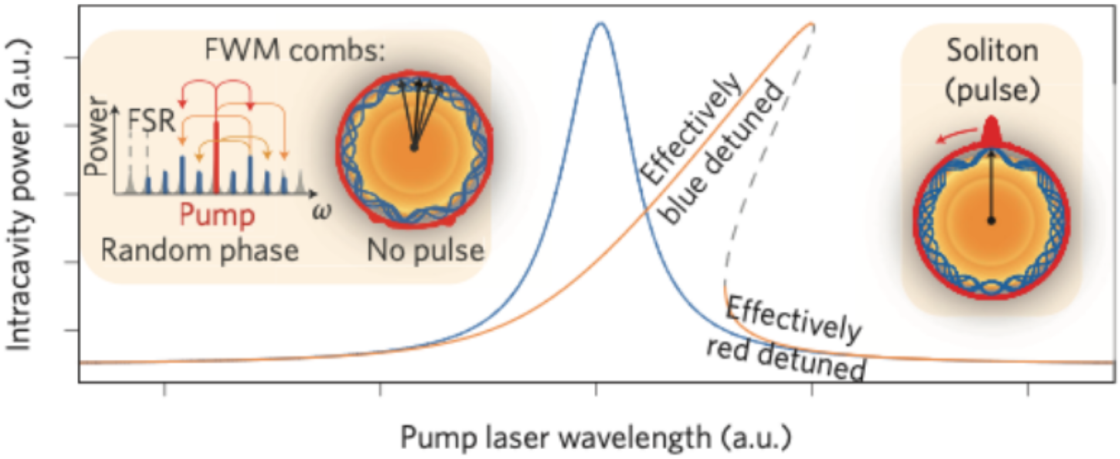

Figure 3.3: Bistability curve shows how the intracavity power changes with laser detuning in a normal resonator (blue curve), and in the presence of thermal effects on the resonance (orange). The increase in temperature in the cavity can move the resonance peak to higher wavelengths, so the Lorenzian shape of the resonance peak will change to a triangle like shape. The left inset shows an FWM comb where the comb lines can remain out of phase, and the right inset shows the soliton generation where comb lines are in phase and synchronized, with a pulsed-like intracavity power. copyright 2014, Nature Publishing Group [12]

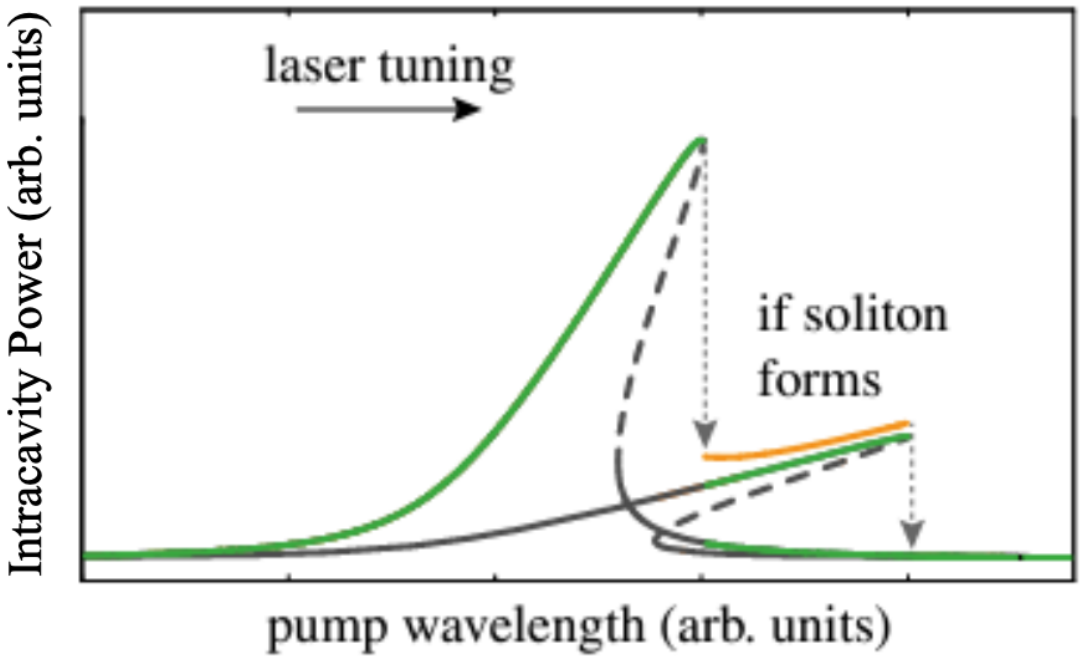

Figure 3.4: The bistability curve showing the steps of soliton generation. The upper branch is effectively blue-detuned and the lower branch is effectively red-detuned. When moving the laser from shorter to longer wavelengths, the intracavity power follows the upper branch of the bistability curve, until it hits a certain value and drops to the lower branch. copyright 2018, The Royal Society Publishing [13]

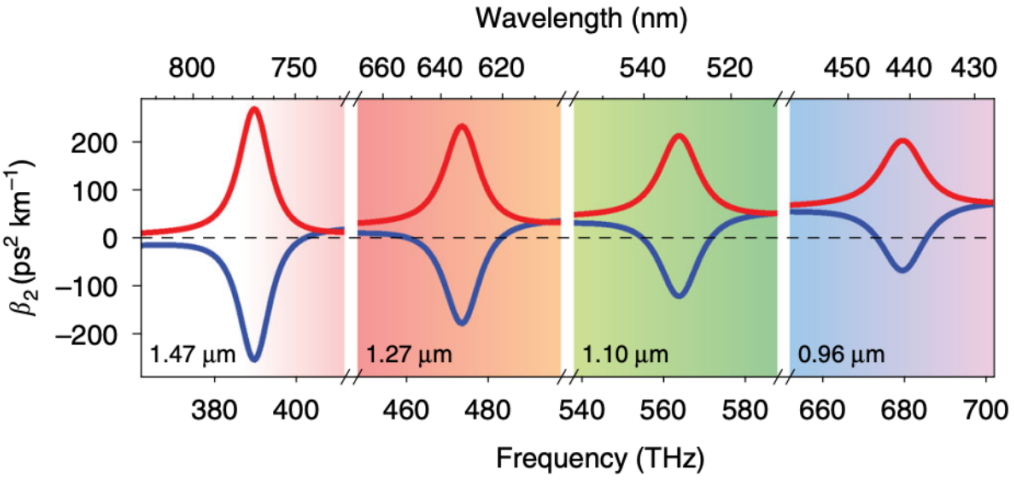

Figure 3.5: Calculated second-order dispersion for two hybridized mode families at different silica microdisk thicknesses. The blue curve shows anomalous dispersion [14]. Copyright Nature Publishing Group, 2017

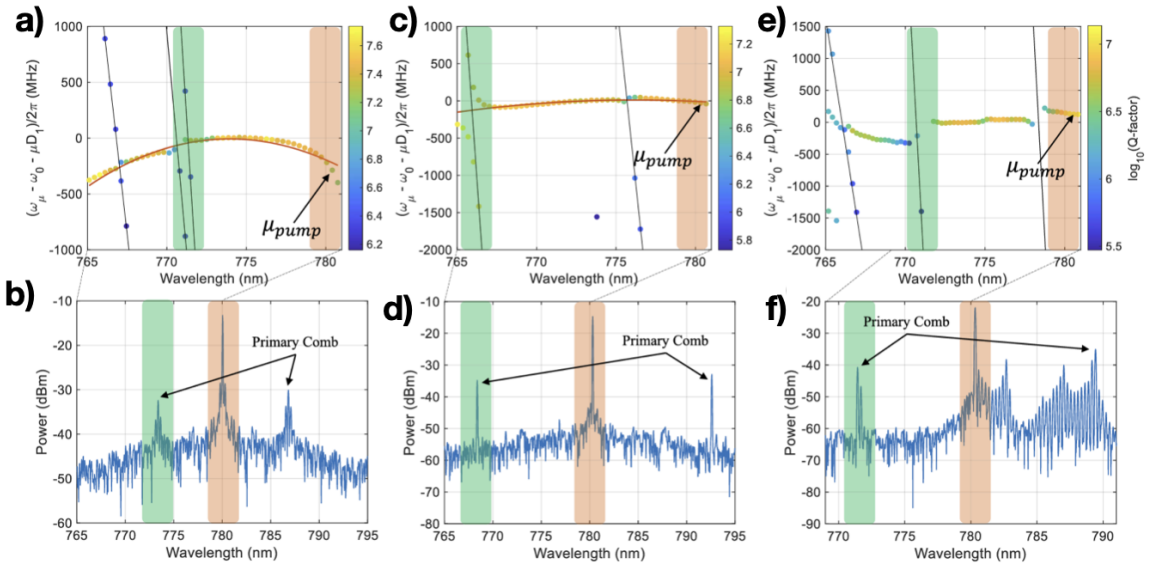

Figure 3.6: The comb generated in water via AMX in near visible wavelength range. B), d) and f) are the comb generated from the pump shown in a), c) and e) respectively. Note that the eigenfrequencies dramatically change and Q degrades when AMX happens. Copyright Optica Publishing Group, 2022 [15]

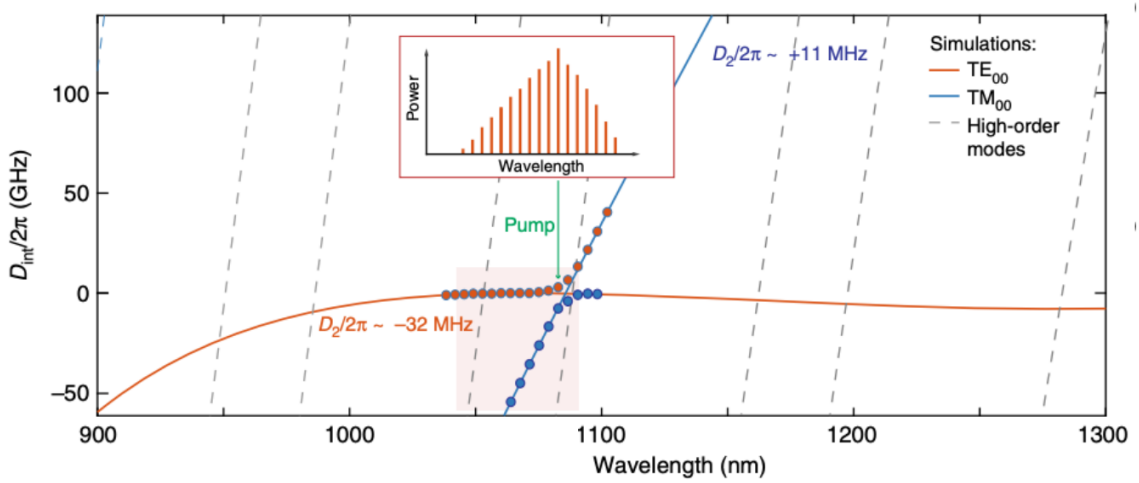

Figure 3.7: AMX for TE00 and TM00 mode families for the microring structure in [16]. As can be seen the local dispersion changes from normal to strong anomalous due to AMX for the TE00 mode, Copyright Nature Publishing Group, 2018

Chapter 4

Fabrication of Ultra-High Q Silica Microdisk Using Chemo-Mechanical Polishing

This chapter is reproduced from [Honari, S and Haque, S and Lu, Tao "Fabrication of ultra-high Q silica microdisk using chemo-mechanical polishing" Applied Physics Letters 119, 031107, 2021, AIP Publishing], with the permission of AIP Publishing.

Over the past decades, the study of whispering gallery mode (WGM) microresonators has dominated many fields of science. Microcavities have become one of the most attractive optical components to study in a broad range of scientific disciplines, including but not limited to, nanoparticle detection, biosensing, quantum information, comb generation, and optomechanics [18, 7, 73, 27, 64, 74]. The power of microcavities to confine the light is mostly measured by the optical quality factor (Q) as the higher the Q goes, the more intense the light inside the cavity becomes [75]. High Q microcavities are essential for better detection in sensing applications, lower threshold power for comb generation and parametric oscillation [33, 76], and narrower

linewidth for laser oscillators [77].

One of the most important limiting factors for achieving high Q is Rayleigh scattering induced by surface roughness [78]. Hence, efforts to increase the optical Q have mainly relied on using sophisticated fabrication techniques such as stepper lithography [17] or CO_2 laser reflow [40] to decrease the surface roughness of microcavities and increase the Q. However, these techniques come with either the need for expensive machinery or incompatibility with monolithic integration. Silica microdisks with Q exceeding one billion have been fabricated recently by carving out the silica and making trenches on grown silica film rather than making stand-alone disks [22]. High Q microresonators and low loss waveguides from other nonlinear materials have also been demonstrated with deposition on silica platforms to take advantage of the smooth surface and low loss nature of the oxide [79].

Chemo-mechanical polishing (CMP) has been used to increase the optical Q for $LiNbO_3$ [80, 48] and Si_3N_4 [47] microdisks, but not for SiO_2 ones. In this paper, we incorporate CMP into conventional photolithography to fabricate ultra-high Q microdisks. Through scanning electron microscopy (SEM), thermal annealing, and numerical modeling, we analyze limiting factors to further Q improvement. It is worth mentioning that the polishing process cannot reduce the roughness underneath the disk. This roughness can result from the dislocations in the silicon wafer underneath the SiO_2, which can make the silica-silicon interface rougher. However, at 10^5 per cm^2 this dislocations are highly unlikely to result in any meaningful impact on Q, since the mode size is about $1\mu m$. In fact dislocation induced roughness anomalies would amount to less than 10 in total in the path of the light inside the cavity.

Our fabrication process consists of four steps: (a) conventional photolithography using deep UV light, (b) wet etching of SiO_2 using buffered HF, (c) chemomechanical polishing of the SiO_2 disks with silica slurry, and (d) XeF_2 dry etch of the silicon

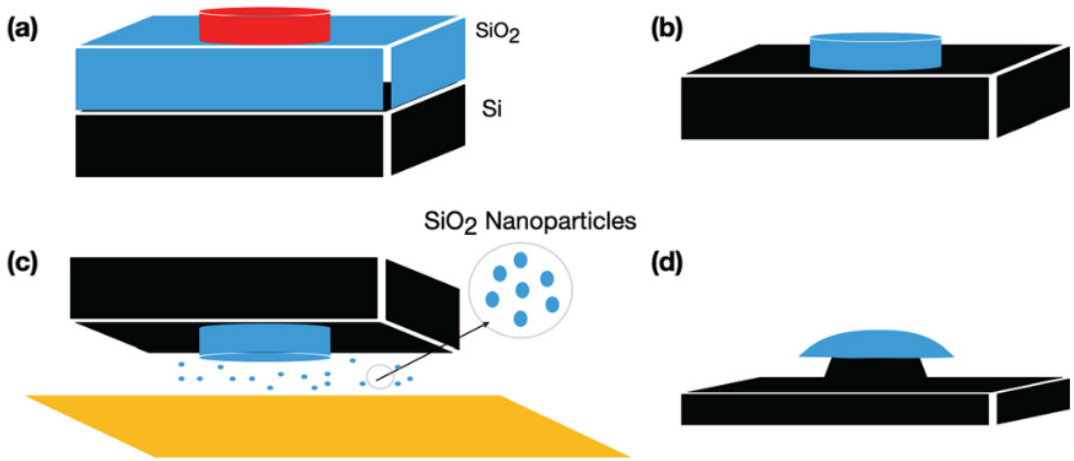

Figure 4.1: Fabrication procedure: (a) photolithography of the resist to transfer the pattern, (b) HF wet etch to make the disk, (c) CMP step to increase the smoothness of the surface, and (d) etching Si substrate to make the pillar.

layer to form the pillars (Fig 4.1).

After applying a standard wafer cleaning process, we spin coat a silica-on-silicon wafer (SoS, University Wafers) with positive resist (S1813). A UV lithography is then applied to transfer the microdisk pattern from the photomask onto the wafer followed by a buffered HF (Transene) wet etch to form disks on the silica thin film. To further improve the surface smoothness of the disks, we proceed to the polishing step using a slurry of 70-nm-diameter silica nanoparticles. Before the polishing step can be done, it is important to change the surface chemistry of the sample. The hydrogen passivation surface of the sample after HF wet etching makes the surface extremely hydrophobic, [81] which can hinder the flow of slurry and reduce the effectiveness of the CMP step significantly. To remedy this problem, we used a 10-minute Piranha solution (H_2SO_4/H_2O_2) to clean the surface and make it hydrophilic. Hand polishing of the sample was then performed using the silica nanoparticle slurry to reduce the surface roughness. In this step, the sample was mounted on a glass slide and was rubbed gently on a polishing pad while adding the slurry on the pad. The pad makes the slurry reach the surface of the disk uniformly. It is worth mentioning that the pad itself is not abrasive and does not polish the surface. The polishing happens by the mechanical impact and the chemical bond formed between the slurry particles and the silica disk. As a result, the sharp edge, which separates the top surface and the sidewall, will be polished away to form a curved contour, as shown in Fig. 4.1(d). Meanwhile, the thickness of the disk was reduced to 7.5 μm from 10 μm after polishing. RCA cleaning steps have also been performed after polishing to wash off the slurry particles stuck to the surface of the disk. In the last step of fabrication, XeF_2 gas was used inside an etching chamber to undercut the disk and form the pillars by etching the silicon underneath the disks. This step is crucial for achieving high Q micro resonators since the light silicon interaction inside the cavity should be

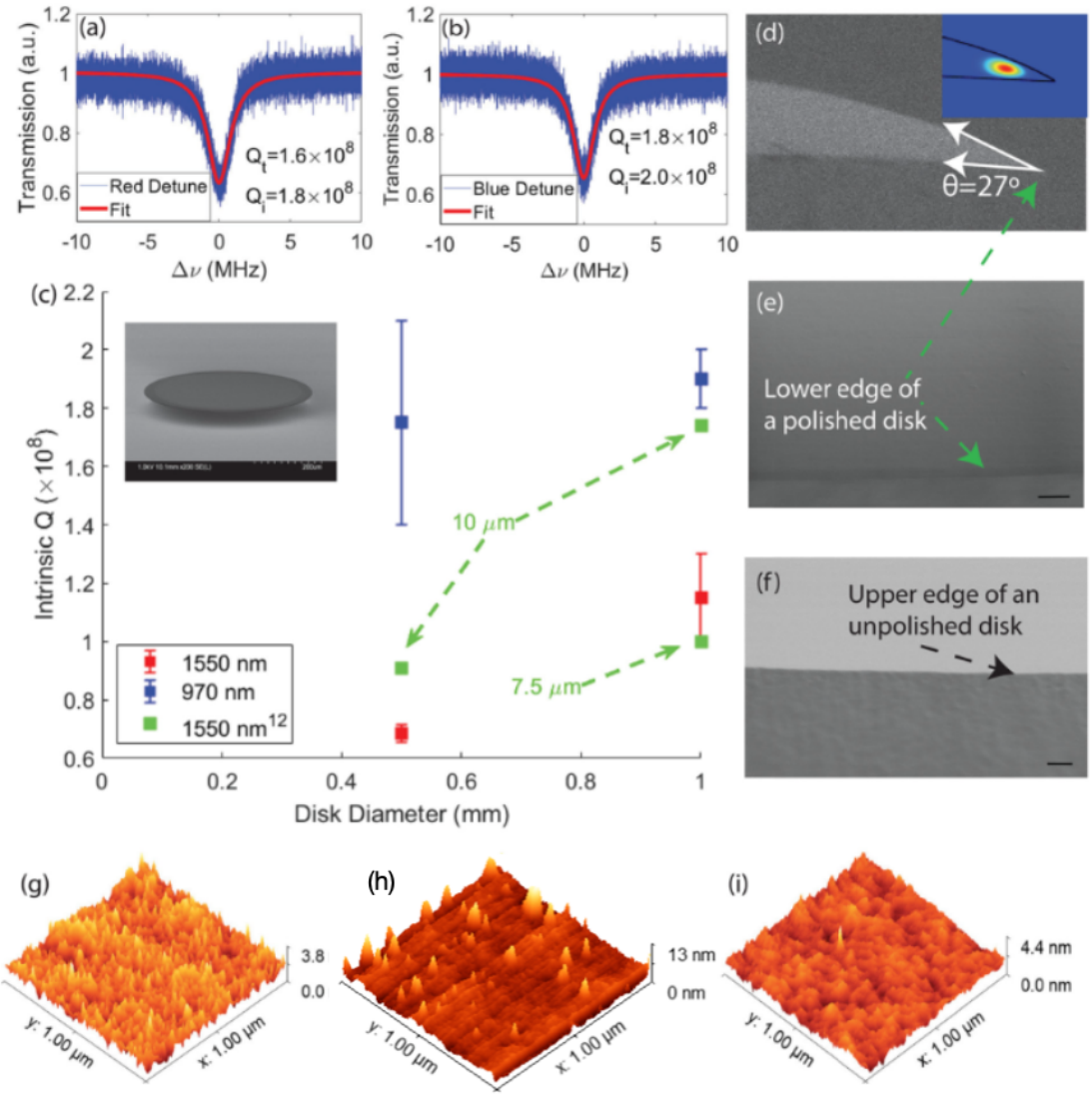

Figure 4.2: Normalized transmission spectra of a 1 mm disk at a whispering gallery mode around $\lambda = 971.32\ nm$ are displayed in (a) and (b). (c) Intrinsic Q as a function of disk diameter at 970 nm (blue squares), 1550 nm (red squares) wavelength bands with the lengths of the error bars corresponding to the differences of the measured intrinsic Q at red and blue detune. In comparison, the recorded values of 7.5 μm and 10 μm thick microdisks by Lee et. al. [17] are displayed as green squares. Note that, after polishing, the silica thin film thickness of our disks reduced from 10 μm to 7.5 μm. (d) The side view SEM micrograph of a polished disk. (e) The top-view micrograph further confirms the upper edge between the side wall and top surface vanishes after polish as opposed to the visible upper edge of an unpolished disk displayed in (f). The atomic force microscope (AFM) micrographs of (g) the edge of a polished disk, (h) the edge of an unpolished disk and (i) the top surface of an unpolished disk show the RMS values of roughness are 0.45 nm, 1.09 nm and 0.33 nm respectively. The black bars on e-f represent 400 nm.

minimized. The maximum amount of undercut is limited by the buckling effect that happens at larger undercuts and can degrade the Q or even crack the disk. However, the problem can be mitigated by high-temperature annealing (1,000 °C) [22].

In the next step, we measure the intrinsic Qs at 970 nm and 1550 nm wavelength bands. Here, external cavity tunable lasers (Santec TSL-550 for 1550 nm, Newfocus TLB 6718-D for 970 nm) were used to probe the microdisks through a tapered optical fiber. As shown in Fig. 4.2(a), by linearly scanning the laser around the cavity resonance wavelength, a Lorentzian-shaped signal will appear at the output transmission of the tapered fiber, from which both total (Q_t) and intrinsic (Q_i) optical quality factors can be calculated. Here, to accurately measure the optical frequency, we placed a fiber Mach-Zehnder interferometer in parallel to the microdisk cavity as a reference [7]. It is worth noting that the intrinsic Q obtained from red detune is lower than the actual value due to thermal and Kerr broadening effects while blue detune of the laser wavelengths yields higher-than-actual intrinsic Q readings due to thermal and Kerr squeezing. Therefore, we take the average of both intrinsic Qs as the estimated value of the actual Q_i and their difference as the uncertainty. For example, as shown on Fig. 4.2(a), the Q_i measured from red detune on a 10 μm (7.5 μm after polishing) thick, 1 mm diameter microdisk at a wavelength λ = 971.32 nm was $Q_i = 1.8\times10^8$ while Fig. 4.2(b) shows that from a blue detune measurement the Q_i of 2.0×10^8 was obtained. Consequently, we determine the intrinsic Q to be $(1.9 \pm 0.1)\times10^8$ as shown in Fig. 4.2(c) (the rightmost blue square with the error bar representing the uncertainty). We also used our fabrication process to make 500 μm disks, and the average intrinsic Q of $(1.8\pm0.4)\times10^8$ was obtained. To better compare our work with previously reported results [17] (green squares), we used 1550 nm laser to measure the Q as well. We observed the optical Q drops to $(1.2 \pm 0.2)\times10^8$ for 1 mm disk and $(6.9 \pm 0.3)\times10^7$ for 500 μm disk (red squares in Fig. 4.2(b)). Note

that the Q of our 1 mm disk is slightly better than the equivalent 7.5 μm thick disks reported in [17]. The side view and top view SEM micrographs in Fig. 4.2(d)-(e) show reduced roughness on the polished disk edge compared to the unpolished one shown in Fig. 4.2(f). An atomic force microscope (AFM, Agilent 5500) was also used to measure the smoothness of the surface. The root mean square (RMS) value for surface roughness decreases from $\sim$1.09 nm for an unpolished disk (Fig. 4.2(h)) to $\sim$0.4555 nm for a polished disk (Fig. 4.2(g)) at the edges. It is worth mentioning that the measurements were on $1\mu m \times 1\mu m$ areas and the RMS value at different locations may fluctuate. As a reference, we also scanned the top surface of the unpolished disk which has been pre-polished by the wafer supplier (Fig. 4.2(i)) and obtained an RMS value of 0.3358 nm, indicating that our polishing procedure resulted in a surface only $\sim$25% rougher than the industry standard. This confirms that our process makes the disk more smooth at the edge and will reduce the Rayleigh scattering. Meanwhile, as shown in Fig. 4.2(d), CMP polished away the sharp angle between the side wall and the top surface, leaving a curved contour on the disk edge.

Further, the observation of lower Q at 1550 nm suggests Rayleigh scattering is not the dominant factor for Q degradation at that wavelength. Instead, water absorption at the disk surface limits the Q since otherwise, surface roughness induced Rayleigh scattering should make the Q at a shorter wavelength (970 nm) even lower [49]. In addition, water from the ambient air can easily stick to the surface of our polished disk since it is hydrophilic after Piranha treatment. Thus, unlike previous observations that Q at 1550 nm is limited by surface roughness, [19, 82, 83] water absorption appears to be the limiting factor for Q in our case because of the different surface functionality.

For further verification, we measured Qs of another disk using 635 nm, 970 nm, and 1550 nm lasers at which wavelengths the water attenuation coefficients are

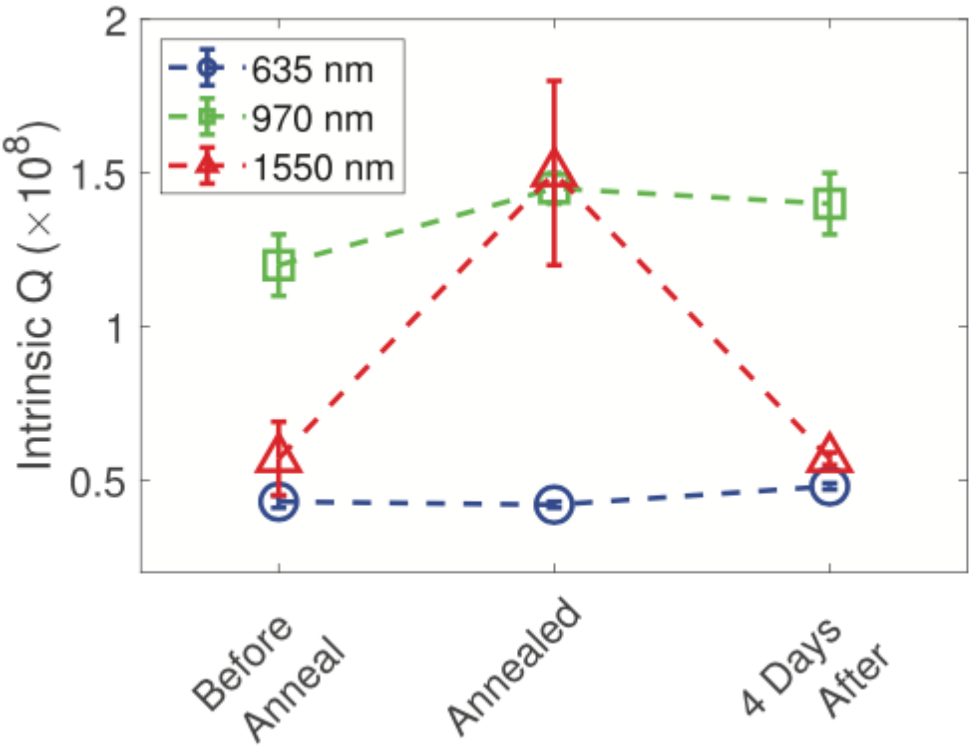

Figure 4.3: Intrinsic Q at 635 nm (blue circles), 970 nm (green squares), and 1550 nm (red triangles), measured before annealing, within 15 minutes after annealing, and 4 days after annealing.

2.79×10^{-3} cm^{-1}, 0.499 cm^{-1} and 12 cm^{-1} respectively [84]. As shown in Fig. 4.3 (labeled as "Before Anneal"), the intrinsic Q values of $(4.3 \pm 0.2)\times10^7$, $(1.2 \pm 0.1) \times 10^8$ and $(5.7 \pm 1.2) \times 10^7$ were obtained respectively. In this case, at 635 nm, the intrinsic Q is approximately three times lower than that at 970 nm, which is consistent with the λ^3 dependence [49] of the surface roughness limited intrinsic Q. At 1550 nm, the lower intrinsic Q again violates the surface roughness limited assumption and suggests a dominant water absorption. To confirm the impact of the water layer, we annealed the disk at 1,000 °C in an ultra-high purity nitrogen atmosphere to remove water molecules and measured the Q immediately after (within 15 minutes after taking the microdisks out of the chamber). As shown in Fig. 4.3 (labeled as "Annealed"), at 1550 nm, Q_i increased significantly to $(1.5 \pm 0.3) \times 10^8$ while its value at 970 nm increased slightly to $(1.45 \pm 0.05) \times 10^8$. Note that, at 1550 nm after anneal, Q is only slightly higher than at 970 nm. Assuming λ^3 dependency [49] of the Rayleigh scattering induced Q (Q_{ss}) is still valid and $Q_{ss} \sim 1.9 \times 10^8$ at 970 nm, one would expect $Q_{ss} \sim 7.8 \times 10^8$ at 1550 nm, which is much higher than the measured Q. This is possibly due to the rapid deposition of a minute amount of water on disk surface during the 15 minutes before the measurement was taken, which starts to accumulate on the surface within minutes after exposure to air [83]. Meanwhile at 650 nm, $Q_i = (4.2 \pm 0.1) \times 10^7$ remains almost the same as before annealing. We further repeated the Q measurements 4 days after annealing. As expected, the re-accumulated water layer on the disk degraded the intrinsic Qs to $(4.8 \pm 0.1) \times 10^7$, $(1.4 \pm 0.1) \times 10^8$, and $(5.7 \pm 0.2) \times 10^7$ at the three wavelengths, which are close to values we obtained before annealing. This again confirms that water absorption is a dominant limiting factor for Q at 1550 nm while it only slightly impacts Q at 970 nm due to the significantly lower optical absorption. At 635 nm, due to the extremely low absorption, the water layer does not cause a noticeable impact on Q. Further,

we can conclude that the water layer at the surface was originated from the ambient air, not from the water molecule trapped in bulk silica dominates the Q degradation since otherwise Q at 1550 nm would not decay to pre-anneal level 4 days after. In summary, the results from Fig. 4.3 help us investigate the origin of the optical loss and Q degradation of our polished microdisks. It can be inferred from the data that the annealing step increases the Q at 1550 nm by decreasing the water content at the surface of the disk. The change in Q is not as significant at 635 nm and 970 nm since the optical loss due to water absorption is limited in those wavelengths.

To estimate the water layer thickness, we numerically simulate the modes and compare the intrinsic Q at both 970 nm and 1550 nm wavelengths. In the simulation, the side view SEM image of the disk in Fig. 4.2(d) was converted to a contour curve for COMSOL simulation as shown on its inset (black trace). In the absence of a water layer, the Q of 2.12×10^{10} at 970 nm and 2.69×10^{10} at 1550 nm were obtained through simulations (the free spectral range is 0.22 nm at 970 nm wavelength and 0.56 nm at 1550 nm). Since our SEM does not provide sufficient resolution for surface roughness, the simulated Q was mainly silica material absorption limited. We then added a layer of water at the disk surface and obtained a Q of 1.56×10^{8} at 1550 nm when the water layer is 1 nm thick. This is in close agreement with our experiment observation around this wavelength. On the other hand, the simulated Q at 970 nm was 4.14×10^{9} due to the significantly lower water absorption at this wavelength band. As the experimental measurement ($Q=(1.9\pm0.1) \times 10^{8}$) is much lower than the simulation value, we confirm that at 970 nm, Q is still limited by Rayleigh scattering. From these observations, we concluded that at 1550 nm, Q is limited by a 1-nm water layer absorption while at 970 nm surface roughness is still the limiting factor for Q.

4.1 Chemo-Mechanical Polishing

We start this polishing process with 70 nm silica particle slurry. The silica nanoparticles are immersed and stabilized in the slurry solution. The slurry is then poured on a polishing pad and covers the entire pad. Next, the sample is mounted on a microscope slide and is gently pressed against the polishing pad. To uniformly hand polish the sample, the movement should take a figure eight shape. The polishing happens as hard nanoparticles on the pad collide with the surface of the disk and break away the anomalies on the surface. Moreover, the silica nanoparticles can chemically bond to the surface of the disk and atomically remove the SiO_2 from the surface, upon breaking off due to movement. The polishing pad is essential to have a uniform surface finish since it makes the slurry reach the sides and top of the disks uniformly.

Ideally, the force on the sample should be controlled. However, this is not possible in a hand-polishing process. Since there is not much control over this manual process, we can only control the polishing time to determine the smoothness and final thickness of the disks.

In summary, we fabricated microdisks with ultra-high optical Q using conventional photolithography in conjunction with CMP. As a result, surface roughness is not a limiting factor for Q at 1550 nm. The Q at a shorter wavelength can be further improved by using smaller nanoparticles as slurry to achieve lower surface roughness. Surface passivation techniques can also be used to make the surface of the disk hydrophobic and reduce the water absorption to the surface. This can be a permanent solution for the disk to maintain high Q at 1550 nm wavelengths. Through simulation, we further find that by removing the 1 nm water layer at the microdisk surface, a Q value close to 10^9 can be reached at 1550 nm. Further research on applications of the ultra-high Q microdisks, including sensing [25] and comb generation, will be conducted shortly to take advantage of this simple but highly effective procedure for future discoveries in these fields.

Chapter 5

A Novel Buckle-Free Large Rib Microdisk with Sub-Micron Thickness

This chapter has been reproduced using previously published results in [9].

Microcavities with high optical quality factors (Q) have been one of the most sought-after optical structures for many years. With applications ranging from biosensing and nanoparticle detection to quantum electrodynamics and comb generation, these devices have been at the forefront of many scientific endeavours [18, 26, 73, 85, 7, 25, 27, 64, 74]. Among the materials normally used to make microcavities, SiO_2 offers unique advantages. The low loss nature of the thermally grown oxide on top of silicon, and compatibility of the platform with already existing CMOS fabrication technologies, made SoS (Silica-on-Silicon) platform a great candidate for optical devices fabrication [23].

One of the fabrication challenges that reduces the applications of SoS platforms, is the stress build-up at the interface between silica and silicon [36]. The stress arises

from the fact that the two materials have different thermal expansion coefficients. Hence, when cooling down from high temperatures (exceeding 1,000 °C when growing the oxide) to room temperature, significant stress will build up at the oxide interface [86]. This hinders microdisk fabrication by buckling the edges of the disk at high undercuts and deteriorates the quality factor of the disk. This issue is more severe in large disks, which are necessary for dense microcomb generation. Although large ultra-high Q microdisks have been demonstrated without significant buckling problems, these devices were fabricated using thick oxide layers, accompanied by tedious high-temperature annealing cycles to remove the stress [17, 22, 36]. However, there is an increasing interest in thin oxide microdisks, specifically for comb generation applications at shorter wavelengths. Short wavelength comb generation is achievable with thinner microdisks [14]. Multi-layer oxide disks with different wedge angles have been proposed before to control the dispersion [35], but a fabrication procedure for a large thin disk is still missing. It has been shown that, for soliton microcomb generation, the needed anomalous dispersion at shorter wavelengths can only be satisfied with thin oxides [14]. Thus, the need for thin oxide microdisks cannot be overstated. Our goal in this work is to fabricate a buckle-free ultra-high Q large disk with thin oxide, by introducing a new rib geometry. The approach introduced in this work can address the buckling challenge without limiting the size and thickness of the disk and does not require any complicated post-processing. Consequently, the fabricated device maintains a high optical quality factor. This, to the best of our knowledge, is the first time such a remedy has been demonstrated to solve the buckling problem in large thin microdisks.

The proposed rib disk structure is shown in Fig. 5.1a, the thin silica layer at the edge of the disk is supported by a thicker top part with a slightly smaller diameter, which provides sufficient mechanical strength to prevent the thin edge from buckling.

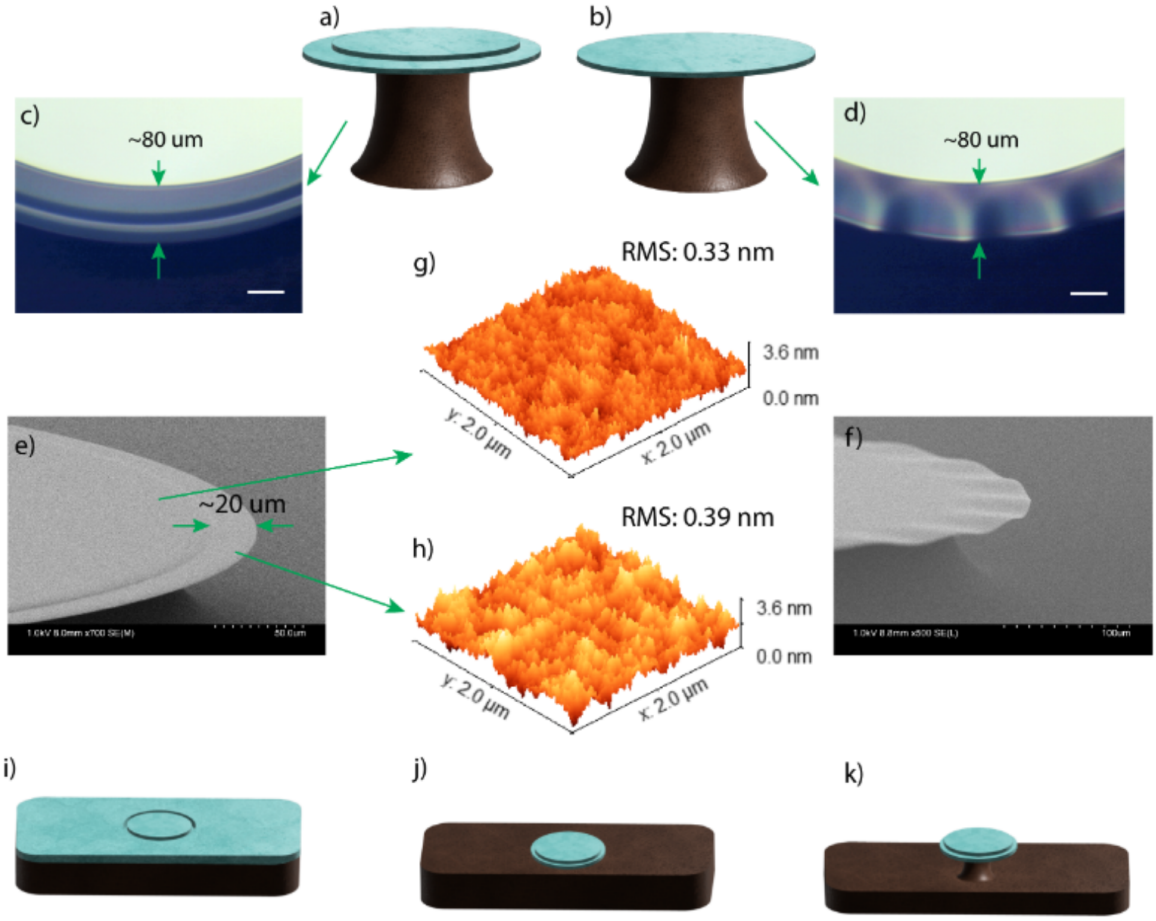

Figure 5.1: A 3-D model of a) the proposed rib disk and b) a regular disk. The top view micrograph c) shows no buckling on the rib disk edge while d) the regular disk with the same undercut ratio is severely buckled. Plot e) further shows the top view SEM of the rib disk. The width of the disk rib is around 20 μm. f) is the SEM image of a buckled regular disk. The AFM images at g) and h) show the surface roughness of the top part and the rib part of the rib disk respectively, RMS values obtained for each part is shown in the figure. Roughness RMS is 0.33 nm for the top part and 0.39 nm for the rib part. i), j), and k) are the fabrication steps of the rib disk. The white bars on optical microscope images are 50 μm each.

In our experiment, we fabricated a 1 mm-diameter disk on a SoS wafer with a 4 μm thick silica thin film. After a chemo-mechanical polishing (see fabrication details in later section), the thickness of the top part is about 3.2 μm while the rib edge thickness reduces to below 1.0 μm (see Fig. 5.2a). The radius difference between the outer ring and the top support (the rib width) is 20 μm to 30 μm (Fig. 5.1e). As shown by the microscope picture in Fig. 5.1c and SEM micrograph Fig. 5.1e, no evidence of buckling was observed even though we undercut the silicon pillar as far as 80 μm. In contrast, a 1 mm-diameter regular disk fabricated on a 2 μm silica thin film[1] (Fig. 5.1b) with the same undercut displays severe buckling as shown in the microscope image (Fig. 5.1d) and SEM image(Fig. 5.1f). Further, we measured the surface roughness of the rib disk using an atomic force microscope (AFM) both at the top and at the rib to see the smoothness of the surface. As shown in Fig. 5.1g-h, the surface roughness RMS value of the top is slightly lower, and is about 0.33 nm , whereas the rib part has an RMS value of 0.39 nm for surface roughness. This small discrepancy can be attributed to the disk geometry before polishing, where the top surface has more contact with the polishing pad due to the height difference between the top and the rib. It is worth mentioning that both roughness RMS values are close to what was obtained in previous works [46]. The AFM data was obtained on a 2 μm$\times$2 μm surface since the rib is not wide enough for large area scans. Such smooth surfaces in combination with the absence of buckles are key to maintaining the high Q of such a large thin disk.

The fabrication process starts with defining a ring on a 4 μm grown silica on a silicon wafer. In order to do so, a Raith 50 e-beam writer is used to define a ring pattern with desired width and diameter, in this case, 980 μm inner diameter and 40 μm width, on PMMA resist, followed by a developing step using MIBK solution.

[1]The disk thickness is around 1.5 μm after polishing.

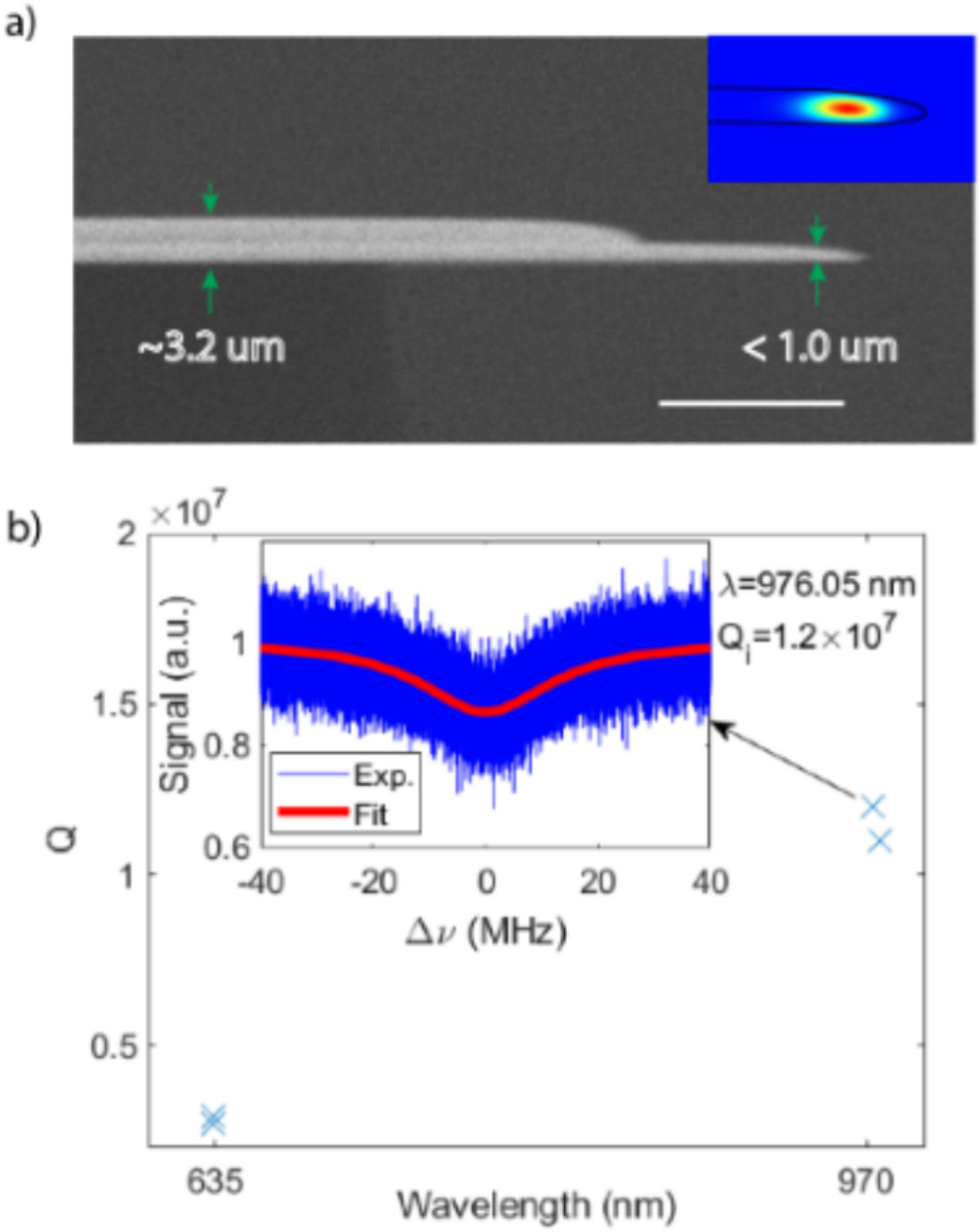

Figure 5.2: a) A side-view SEM image of a rib disk along with the simulated mode profile (inset), The thickness of the rib and top part of the disk were calculated after accounting for a slight slope of the sample. The graph at b) represents optical Q data for two different wavelengths with the normalized transmission spectrum in the inset. The white bar in the SEM image is 20 μm in length.

Then the wafer is wet etched using a buffered HF solution (Transene), to etch away the ring to about 1 μm. The PMMA resist is then washed away with acetone (Fig. 5.1i). The next step is to define the disk on top of the ring. Note that the disk has to partially cover the ring. The overlap region between the two patterns defines the size of the rib. Disks are made using a photolithography step followed by a HF wet etch down to the silicon substrate, and a polishing process to reduce the surface roughness of the disk and boost the Q (Fig. 5.1j). The details of the polishing process have been discussed in [46]. The final step is using XeF_2 to etch the silicon underneath the disk and form the pillars (Fig. 5.1k). Buckling could happen in this last step by reducing the Si/SiO_2 interface and releasing the stress. SEM side-view images and profilometer data suggest the thickness of the disk at the edges is about 980 nm to 1 μm. We then measured the Q at two different wavelengths using a reference interferometer setup described in Ref. [46]. The disk transmission spectrum is shown as the blue trace of Fig. 5.2b inset, which is fitted to a Lorentzian function (red trace of Fig. 5.2b inset) to obtain the intrinsic Q of the cavity. As shown in Fig. 5.2b (blue cross markers), the Q as high as 1.2×10^7 was achieved at 970 μm and 2×10^6 when measuring with a 635 nm laser for this rib disk. The Q degradation at shorter wavelengths can be attributed to more surface scattering at these wavelengths [49, 46], which may be improved through a refined chemo-mechanical polishing procedure. This also suggests that Q will be higher in the aqueous environments, since the surface scattering Q is inversely proportional to the square of difference between the two media refractive indices square, as shown in the equation. 2.3

$$Q_{ss} \propto \frac{1}{(\delta n^2)^2} \tag{5.1}$$

Here δn^2 is $n^2 - {n_0}^2$, where n is the refractive index of the cavity and n_0 is the refractive index of the surrounding environment. In contrast, we couldn't observe

any resonance of the buckled regular disk as these buckles significantly reduce the photon lifetime inside the cavity.

5.1 Buckling Simulation

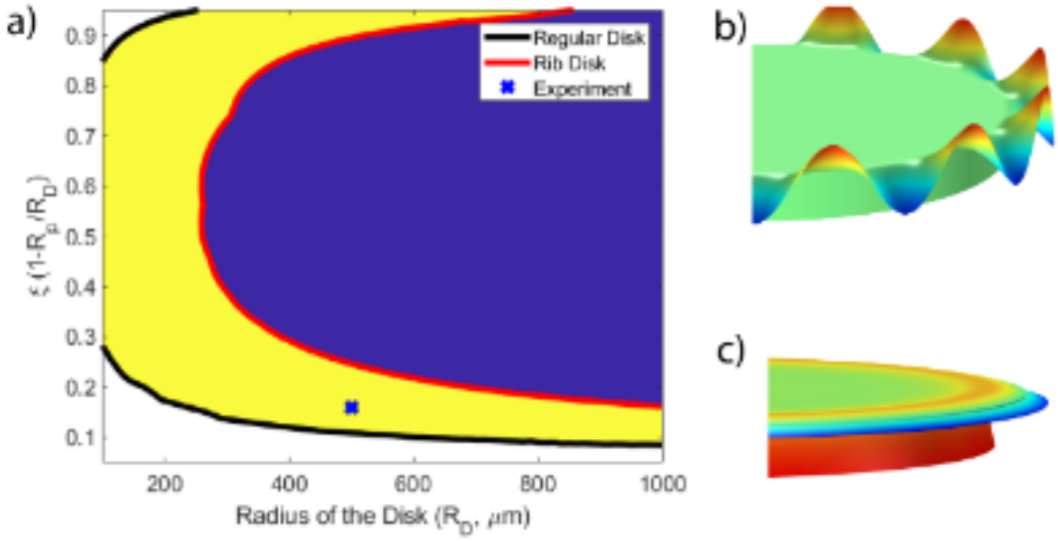

Figure 5.3: a) Buckling threshold for rib and regular disk as a function of disk radius (R_D) and the undercut ratio ξ. The yellow-coloured region in the graph represents the gain in our design, where the rib disk remains mechanically stable, but the regular disk with the same dimensions and undercut buckles, while in the blue-coloured region, both structures show buckling. At the setting ("x" marker), where both disks were fabricated, the simulation b) shows that a regular disk will buckle while a rib disk showing in c) will not buckle.

To further investigate the mitigation effectiveness, we did mechanical buckling simulations on our rib disk and a regular disk with the same thickness and diameter. To model the mechanical stability of our design, the thermal stress induced by different thermal expansion coefficients in silica and silicon is simulated in COMSOL Multiphysics via the finite element method. The linear buckling study in COMSOL is used to derive the critical load factor (CLF). CLF is defined as the ratio of the minimum load for buckling to the existing load. A CLF less than 1 means that the

structure would face instability under thermal stress. The buckling threshold derived analytically in [36] now can be calculated numerically by doing a 2D parameter sweep on disk radius R_D and the undercut ratio $\xi = 1 - R_p/R_D$ defined as 1 minus the ratio between the pillar (R_p) and disk (R_D) radii. It is shown that a boundary between buckled and unbuckled regions can be obtained using numerical simulation on linear buckling for any thickness. This boundary, in our simulations, is defined by the contour of CLF=1.

Our simulation in Fig. 5.3a displays the unity CLF contour of our rib disk (red curve) and a regular disk with the same disk thickness of 1 μm (black curve). In general, the left-hand side of the curve shows critical load factors higher than one, which means the disk remains unbuckled. The right-hand side of the curve shows critical load factors below one, hence the disks will buckle. Consequently, both rib and regular disks in the blue region will buckle. The yellow region in Fig. 5.3(a) shows the area in which the rib disk remains stable, but a regular disk will buckle. Further, in the white region, neither the regular disk nor the rib disk will buckle. The cross marker represents the configuration ($R_D = 0.5$ mm and $\xi = 0.17$) of the regular and rib disk we fabricated (also see Fig. 5.1c and 5.1d). As shown, although the normal disk with the size and thickness specified will buckle (Fig. 5.3b), our rib disk with the same size will remain mechanically stable even at high undercuts (Fig. 5.3c). These simulations are perfectly on par with the experimental results shown earlier.

In conclusion, we demonstrated novel buckle-free rib microdisks with high-quality factors. Using the developed fabrication procedure, a 1-mm-diameter, and < 1 μm thick rib disk at a Q above ten million was demonstrated. With a refined fabrication, our simulation predicts that a larger and thinner buckling-free high Q disk can be made. In future research, such rib disks will be developed to dense soliton microcombs at visible wavelengths that may enable in-vitro label-free single molecule spectroscopy.

In addition, the rib structure can be directly adapted to other material platforms such as SiN, $LiNbO_3$, etc. to make large disks with enhanced mechanical rigidity. More importantly, as a novel cavity structure, many photonic properties are yet to be explored. In the following chapter, we utilize the structure introduced here to generate comb at short wavelength (780 nm), we showed the rib disk structure can generate comb both in the water and in the air.

Chapter 6

Frequency Comb Generation in Short Wavelengths

Different applications of WGM microcavities have been extensively investigated in the past [18, 87, 7, 25, 88]. Among these applications, microcomb generation has emerged as one the most sought-after areas of non-linear optics research [89, 90]. With applications ranging from optical clocks to sensing to quantum computing, microcombs have brought significant impacts to the fields in optics [64, 91, 92, 93]. One of the challenges for comb generation has remained the anomalous dispersion, needed to satisfy the nonlinear Schrodinger's equation for bright solitons [12]. This is an even bigger challenge when trying to generate soliton microcomb at shorter wavelengths [14]. Micorcomb generation at visible wavelength has huge potential, especially for applications in aqueous environments and biological samples [16]. Hence, a lot of effort has been invested to solve challenges related to comb generation at short wavelengths and ultimately in water [14, 16, 15, 94]. Visible comb generation using silica WGM microcavities has been achieved with geometrical control of the microcavity to achieve geometry-induced anomalous dispersion [14, 61]. Other platforms

like Si_3N_4 were also used for short wavelength comb generation [94, 16], but lower Q of microcavities compared to their silica counterparts can make comb generation using these platforms more challenging. Here we demonstrate bright and dark soliton comb generation using a silica rib disk, with highly dense comb lines at 780 nm wavelength, using transverse modes interaction.

Comb generated by different transverse mode families have been reported before [95] with higher FSR than the combs generated from the same mode families. As can be seen in the Fig. 6.2, the comb generated using the rib disk can have smaller FSR down to 10 GHz for both 1 mm and 500 μm disks. This is a result of the closely packed transverse modes in our rib disk, due to the significant reduction in the thickness of the disk. Here we use rib disks with two different sizes to generate microcomb both in the air and in DPBS solution. As mentioned, the teeth spacing in the comb is about 20 times smaller than azimuthal modes FSR. Hence, the resulting comb lines are not generated by the azimuthal modes. Interestingly, the mode spacing does not change by changing the size of the disk, which also shows the generation of the comb by transverse modes. Moreover, we could find modes responsible for comb generation by simulating the modes in the desired wavelength window for each structure.

To do that, a profilometer scan of the rib disk 6.1 was fed into COMSOL mode solver to generate the modes available. The result was then used to find anomalous dispersion between the modes that can generate combs with the observed spacing. As shown, modes with both anomalous and normal dispersion could be found satisfying the spacing conditions, which could mean the existence of both dark and bright soliton is possible in the rib disk. Although co-propagation of dark and bright solitons was investigated both theoretically and experimentally, [96, 97], these reports use different wavelengths to generate comb in anomalous and normal regimes. Here we capitalize on the transverse mode generated comb, which can have both anomalous and normal

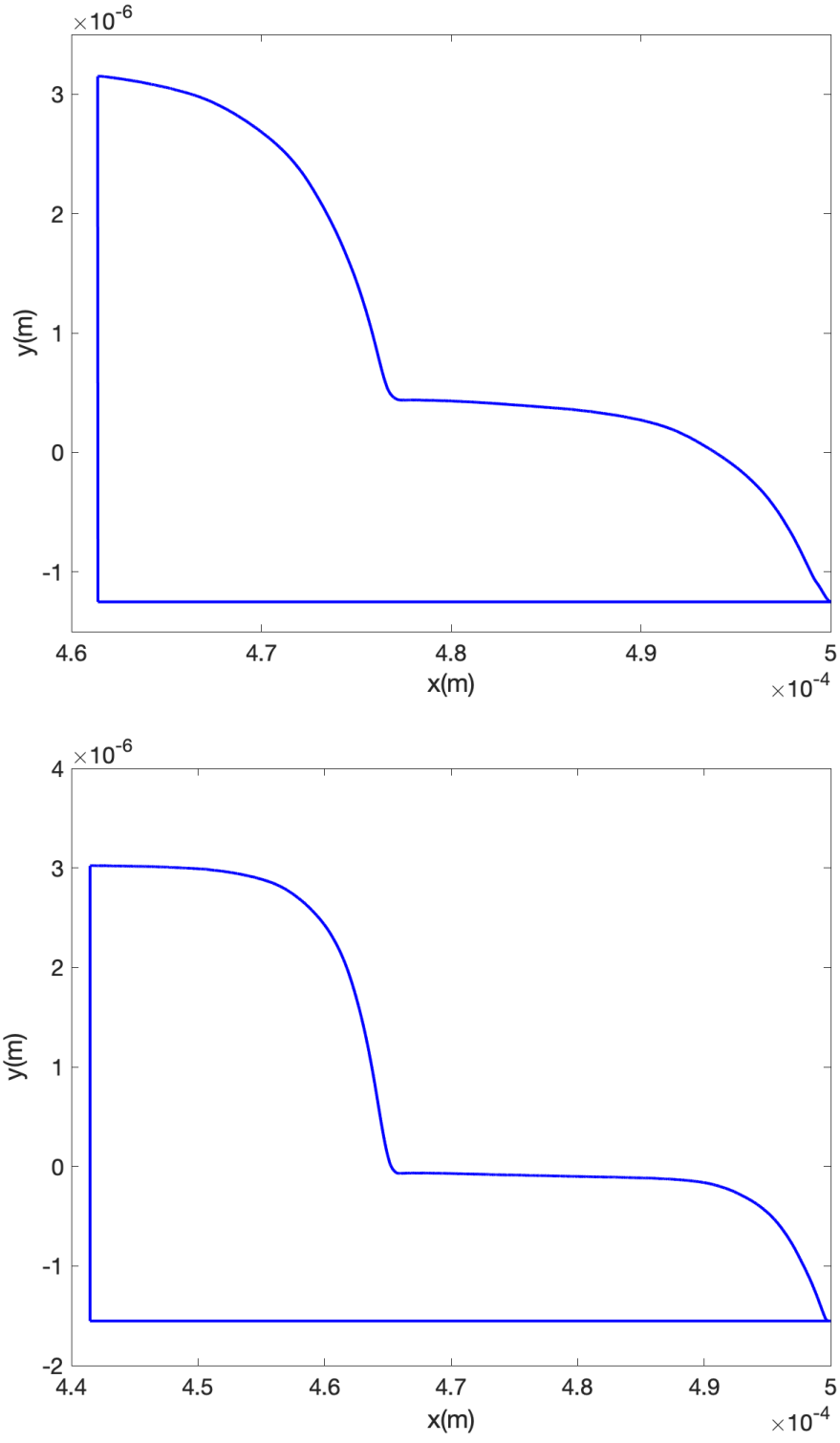

Figure 6.1: The profilometer data showing the side view of the rib disk for 12 minutes polish (top), and 15 minutes polish (bottom), used to simulate the modes .

dispersion depending on the participation modes. Dark solitons can also be generated without a threshold power [98], which is a huge advantage. As can be seen in 6.1, different polishing runs can lead to different side-view images of the rib disk. However, in both cases, there is an obvious curve in the sidewall, which makes finding a wedge angle very difficult, since the sidewall is gradually and non-linearly getting thicker. The hand polishing method we use is prone to be unreliable. The force applied to the sample while polishing and the polishing speed would definitely play a role in the final sidewall shape, and controlling them in hand polishing is not an easy task. We are looking to automate this process using a polisher to have better control of the sidewall and thickness of the final rib structure.

The optical spectrum analyzer (OSA) spectrum shown in 6.2 is what was observed when we coupled light into the rib disk. To do so, we used a 1550 nm laser in scanning mode to generate the 1550 nm light. The light was then amplified using an Er-doped fiber amplifier, which then went through a second harmonic process inside a $LiNbO_3$ frequency doubler to generate 775 nm light (the schematic of the optical setup is shown in Fig. 6.7). The 775 nm output is about 150 mW. The OSA data at Fig. 6.2 shows the comb lines beginning to form out of the main laser peak, the distance of the sidelines from the main line is the same in each case which means the conservation of energy is satisfied for the process both in the water and in the air.

Two observations show these comb lines are not necessarily the conventional comb that has been reported before. The first observation contrary to the conventional comb was the spacing of the comb lines. The comb lines in the spectrum are far denser than one FSR and seem to be the same regardless of the size of the disk. We observed the same spacing of about 0.01 nm for both 1 mm and 500 μm disks. This shows the modes responsible for the comb generation are not in the same family with different azimuthal mode orders. Computer simulations of the possible modes

in the disk showed us that because of the small thickness of the disk, especially at the edge where different transverse modes are very close to each other and there is a possibility of having them coupled into each other. Further expanding the simulations into other wavelengths gave us a better understanding of different modes inside the cavity (Figs. 6.3 and 6.4). By carefully evaluating the possible modes, we could find certain transverse modes satisfying the anomalous dispersion and with the spacing observed in the OSA data.

The second observation was about the conservation of momentum in the process. Traditionally the momentum has been equated to $\frac{M}{R}$ for modes in a WGM microcavity. However, this definition would not necessarily hold for every situation [95]. In the case of the comb generation via adjacent azimuthal modes, all the modes would have momentum in the same direction, which means the angle of momentum is the same for every one of them. Thus, the conservation of momentum is simply making sure the momentum values stay the same before and after the process. In the case of modes from different transverse families, the angle of momentum might not necessarily be the same so the conservation of momentum relies on the vector sum of the momentum of the photons before and after the process. Hence, the value of the momentum might not necessarily stay constant. This has been also observed in [95], for cylindrical shape microcavities.

In the final part of this chapter, the optical setup and the Q measurement scheme would be explained.

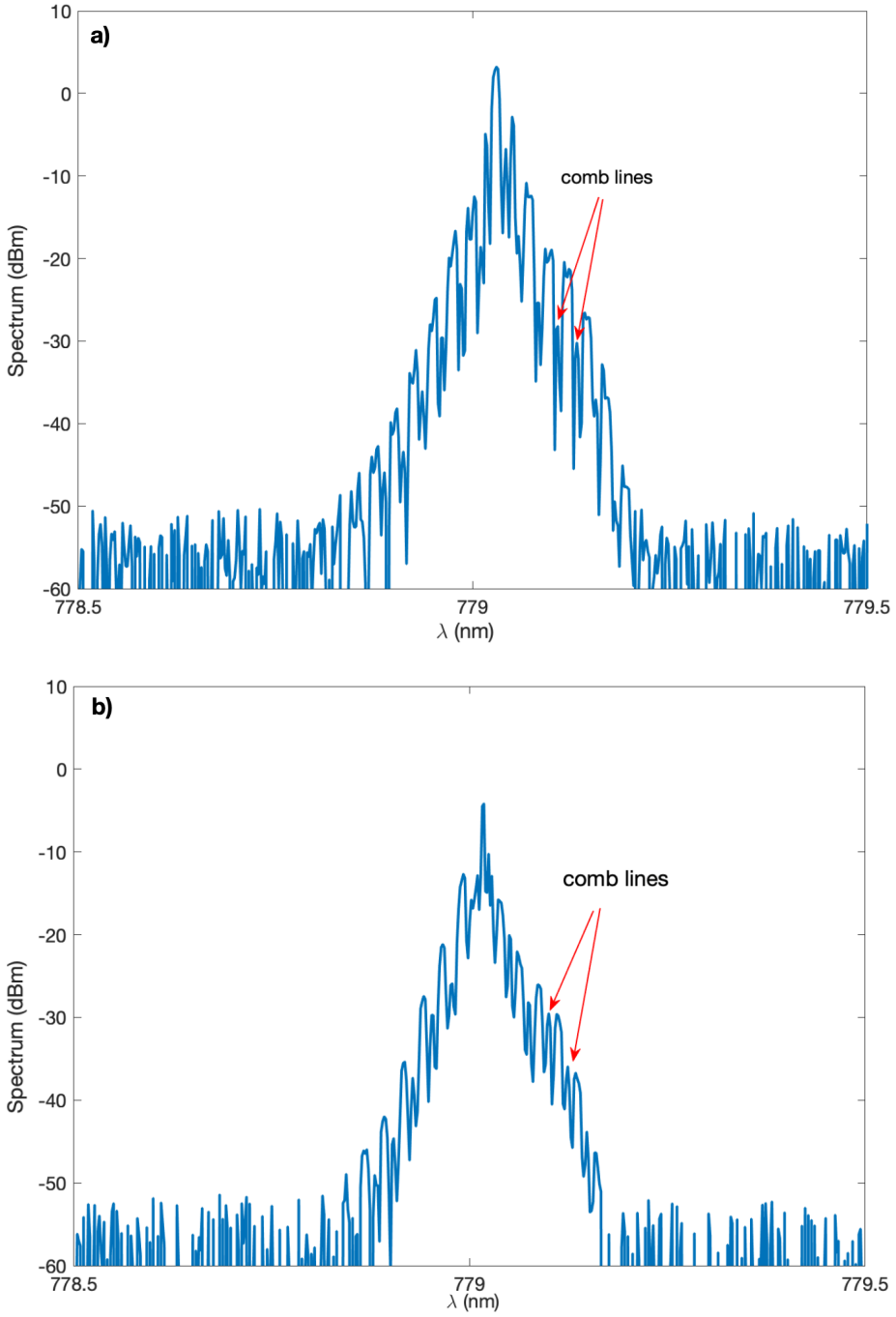

Figure 6.2: Comb lines generated in a rib disk through FWM process, in the air(a), and DPBS solution (b). The spacing in both cases is about 0.01 nm

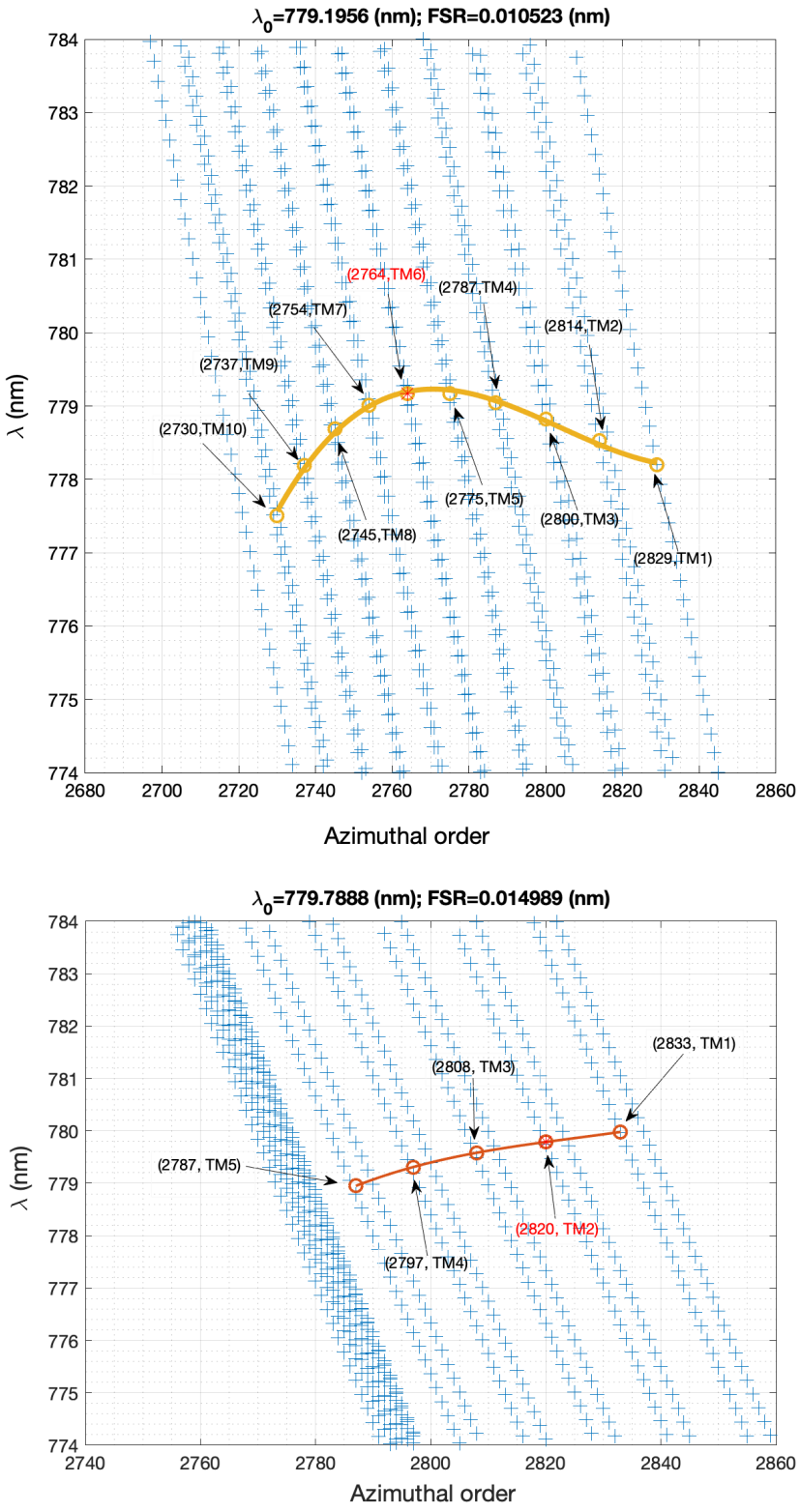

Figure 6.3: Modes responsible for comb line generation in the air (top), and in DPBS(bottom) with the observed 0.01 nm spacing

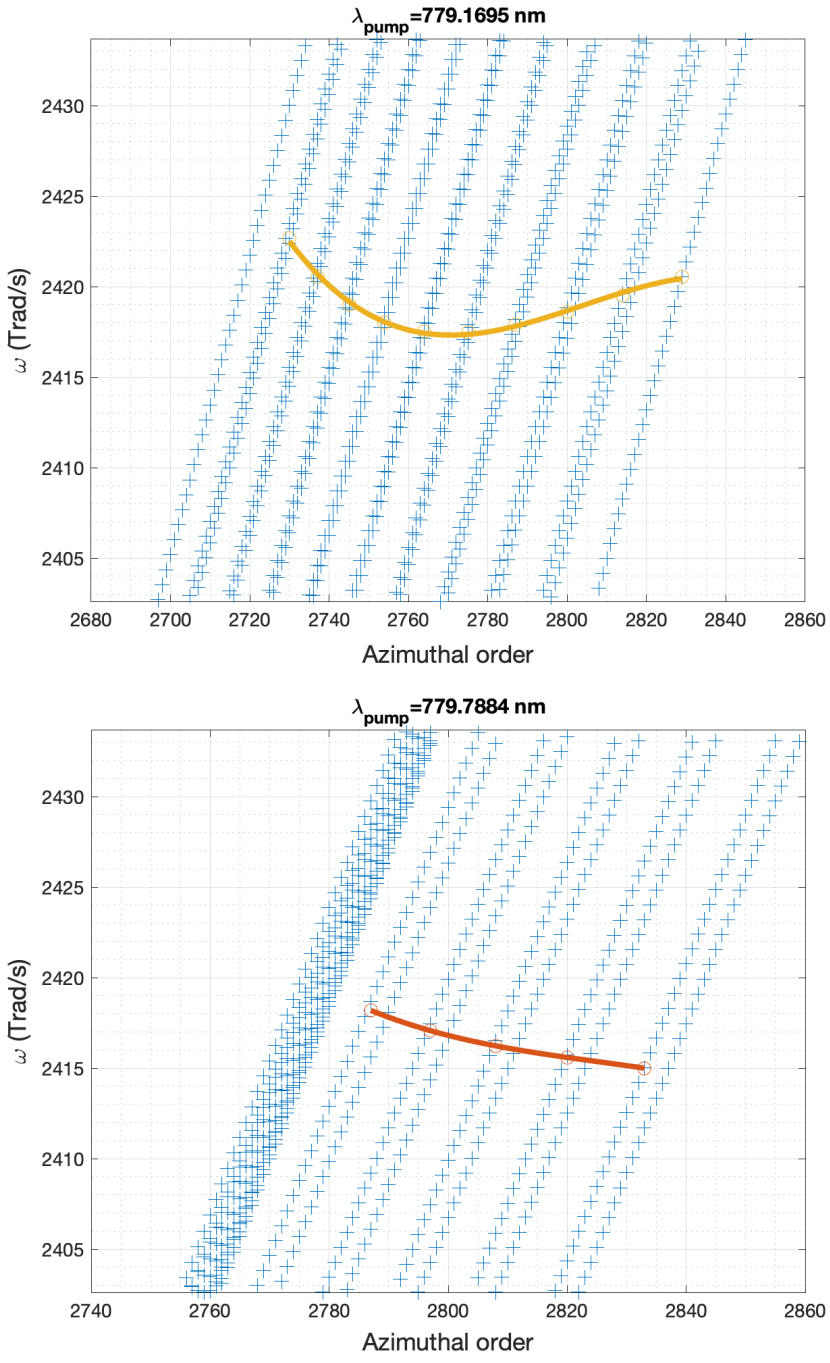

Figure 6.4: Same as 6.3, but for ω vs azimuthal mode order. The top image is for modes generated in the air and the bottom image is for the modes generated in water

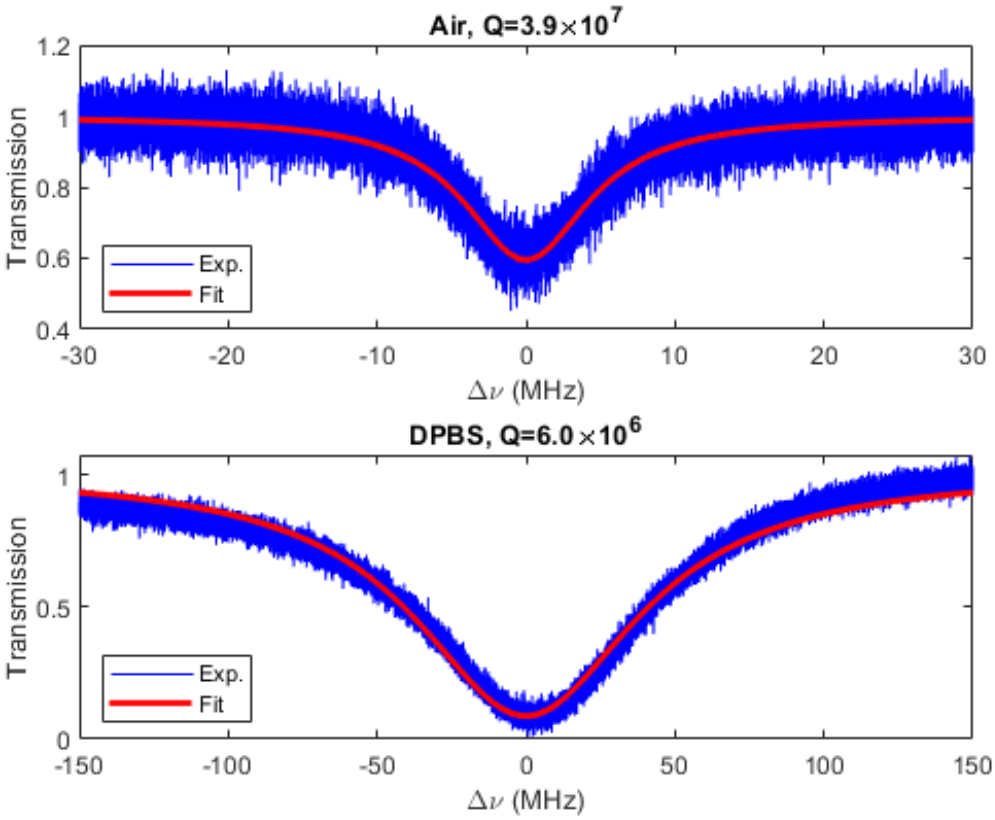

Figure 6.5: Q measurements in the air (top) and in DPBS solution (bottom). the measurements confrim high quality factors can be achieved in both media using the rib disk.

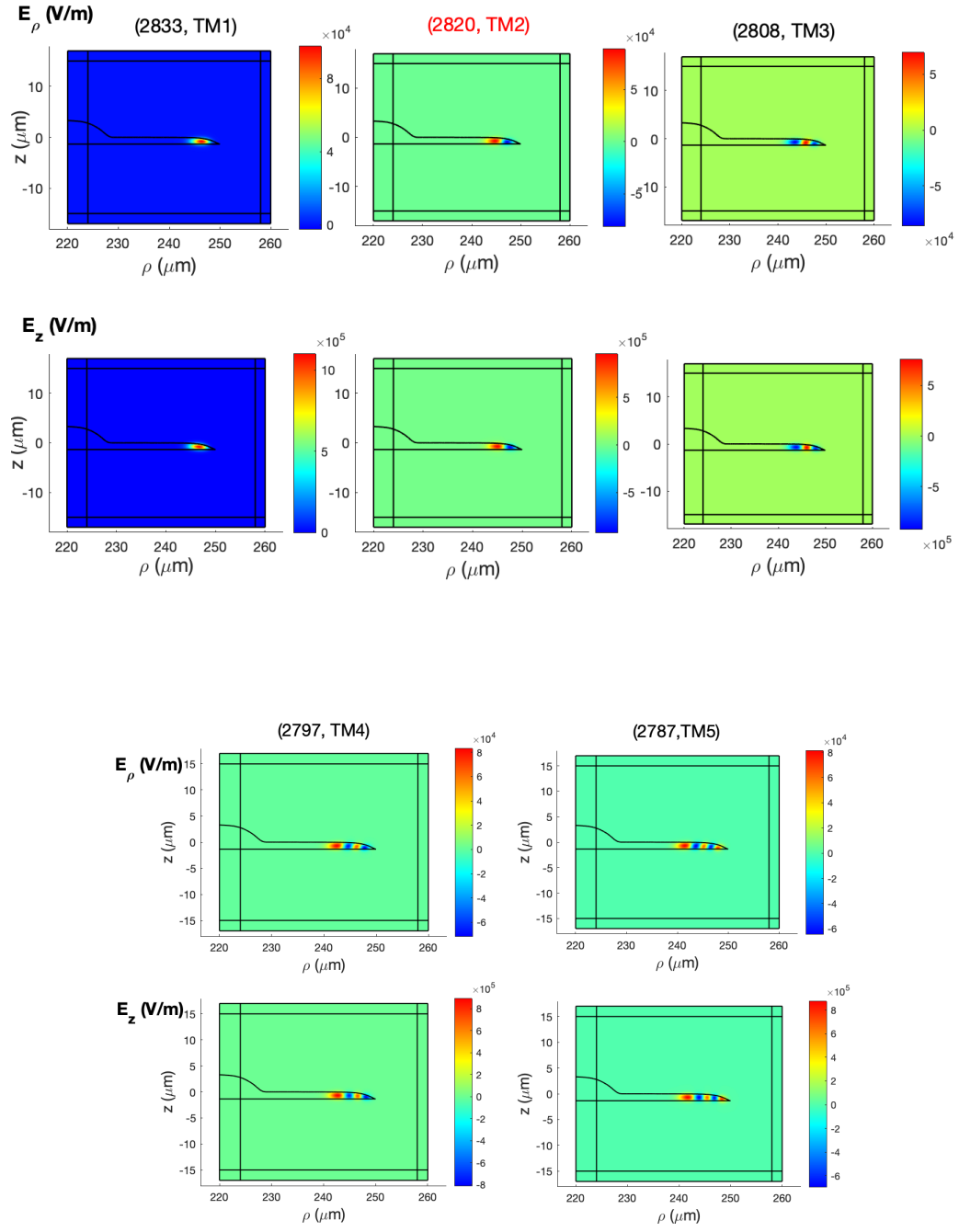

Figure 6.6: The modes responsible for the curve found in Fig. 6.3 in DPBS, the azimuthal mode number increasing does not remain constant. This can be explained by the difference in the angle of momentum for different transverse mode families.

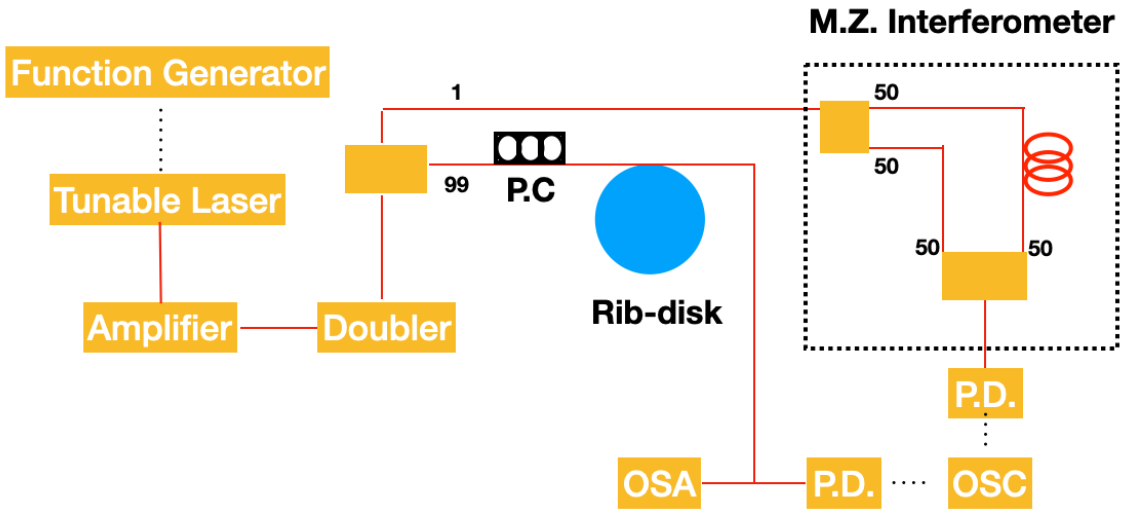

Figure 6.7: The optical setup used for comb generation and Q measurements, a tunable laser is amplified at 1550 nm wavelength, and a $LiNbO_3$ frequency doubler is used to generate 775 nm wavelength. The light is coupled to the rib disk through a tapered fiber.

The optical setup (as can be seen in the schematic of Fig. 6.7) consists of a laser, an amplifier, a frequency doubler, an interferometer, an optical spectrum analyzer, and an oscilloscope. To couple the light into the disk, we use a single-mode fiber, and pull it to desired thickness using a hydrogen torch. The thickness of the fiber affects the coupling efficiency of the light into the cavity.

The 1550 nm light generated from the laser will go through an Er-doped fiber amplifier and then through a frequency doubler to produce 775 nm light. The 99/1 coupler divides the light into two branches, one will go through the interferometer and the other branch will be coupled to the disk. The output of the tapered fiber would be connected to the OSA and OSC. The M.Z interferometer is used to generate a sinusoidal reference signal when scanning the wavelength of the laser. We use this reference signal to measure the full width at half the maximum of the resonance peak to measure the quality factor. The power inside the cavity will be lowered by under-coupling of the light for Q measurements to avoid thermal broadening. However, we

tried to achieve critical coupling while generating comb lines. The setup was taped to the optical table to make it stable, and all the fiber heads were cleaned and evaluated for any damage or dust accumulation before connecting them to high power.

Chapter 7

Summary and Future Works

In this chapter, a summary of the whole document will be presented along with potential future work. As mentioned in previous chapters microcavities and microdisks, in particular, can have a huge impact on the vast number of applications such as comb generation and sensing. Moreover, using silica on silicon as a platform is proven to be cost-efficient and easy to produce, given the rich history of CMOS fabrication technologies. Thus, we chose to work on silica microdisks and improve the quality and performance of such disks for future applications.

The first hurdle was the Q value. In general, the optical quality factor (Q), needs to be boosted to improve the performance of a microdisk, whether this performance is the threshold power for comb generation or the sensitivity of an optical sensor. So, our first task was to tune the fabrication process to increase the Q. The technique used for this part of the project was to add a chemo-mechanical polishing (CMP) step in the process to decrease the surface roughness. By doing so the RMS roughness was decreased significantly (from 1.09 nm to 0.45 nm). Furthermore, the addition of this step made thorough cleaning of the sample an even bigger priority, since the CMP process is dirty in nature. So, developing a new cleaning procedure was of

great interest. The cleaning process was developed using a combination of the RCA cleaning process and Piranha cleaning. Finally, the Q values over 10^8 were reported. Moreover, it was demonstrated that the surface roughness is no longer the limiting factor for Q at longer wavelengths, but the water absorption at the surface is what limited the Q. It also showed us that by tuning the CMP process, like using smaller particle size for slurry and using the polisher machine instead of hand polishing, Q can be further improved.

Q was not the only problem we were facing. We knew that for comb generation certain structural changes need to be made on a microdisk to have anomalous dispersion. One such change was the decrease in the thickness of the disk to induce mode hybridization inside the cavity to have the required dispersion. However, this comes with significant challenges. Firstly, thinner disks tend to have lower Q, which worsens the performance. Secondly, thin disks tend to buckle under the stress after undercut. The stress arises from the fact that silica and silicon have different thermal expansion coefficients, so when the wafer cools down after the growth, the stress builds up at the interface. This stress is released after the undercut in the form of buckling the top silica if the disk is thin enough. So far, this problem prevents the fabrication of large-diameter disks, and researchers have to stick to less than 100 μ disks to ameliorate the buckling problem. However, this disk size is not suitable for dense microcomb generation, since the teeth spacing is inversely proportional to the disk size. To solve this problem a new rib structure was introduced for the microdisks, with thin edges and a thick middle part. Mechanical stability was demonstrated even at high undercuts and thin disks. A thickness of less than 1 μm was possible for the disk using this structure. Both simulation and experimental data shown in previous chapters evince the mitigation of buckling in our new structure. Moreover, using the previously developed CMP process, Q got boosted to more than 10^7. This, to the

best of our knowledge, is the thinnest silica microdisk, with the largest diameter ever made. The final step was to couple 778 nm laser into the disk and see the response. We used a $LiNbO_3$ frequency doubler to convert 1550 nm laser to 775 nm. The 1550 nm laser was amplified using an Er-doped amplifier to achieve higher powers. What we measured out of the OSA seemed to be the onset of a four-wave mixing process to generate a comb. However, the mechanism by which the comb is being generated is probably different than most reported combs. In this case, we see comb being generated by different transverse mode families, rather than different azimuthal modes. That is why the comb spacing is very narrow, and the size of the disk does not change it. The soliton comb generation in a locked laser scheme is yet to be materialized in our experiment.

All the efforts invested into this project were necessary to generate microcomb at visible wavelength, and the main reason for microcomb generation at the visible range is to do sensing in water. Hence, naturally, these would be the next steps of future work.

The next phase of the project will be to generate microcomb at visible range. To do that, we are going to use our current fabrication technique and novel structure, which has anomalous dispersion based on the simulations and calculations done in this group and others. Although our fabrication process is quite mature, further tuning the polishing recipe might be needed to achieve higher Qs, since the short wavelength Q is highly dependent on the surface roughness. Nevertheless, the fabrication techniques and expertise developed in this group should be quite helpful for the next phase of the project. Also, our techniques let us explore increasing the microdisk size, to have a denser comb.

There could be some challenges in our way in this phase of the project. Firstly, there is a need for high-power laser for comb generation. Although the Q can sig-

nificantly affect the threshold power needed for comb generation, higher powers are needed for wide-span comb generation. Also, the formation of soliton inside the cavity can be challenging. Although theoretically, comb generation is possible in a nonlinear medium with anomalous dispersion, this needs very careful tuning of the setup. The visible comb generation can be a huge milestone in our project since no one has ever done that. Generation of soliton also requires a careful locking of the wavelength using a lockbox. The scanning wavelength meaurement that we have used so far can add to uncertainties and errors in the measurements.

The second phase of the project would be using a visible comb in water for sensing. The main justification for choosing this particular application is that water does not absorb visible light. So, the Q would remain intact, which is a huge advantage over longer wavelength microcombs. Furthermore, by having shorter wavelengths, we can explore a vast number of molecules or even reactions with energy levels higher than infrared. The experimental setup and expertise exist in the group since other in-water particle sensing projects were implemented in the group. So, we expect this step to be less challenging and probably faster.

Finally, we consider pursuing other applications using the platform we developed. Because of the irregular edge shape and the thickness of our rib disks, we can achieve higher light-surface interaction through the devices. This can potentially increase the chance of particle sensing or even second harmonic generation since second harmonic generation in silica happens at the surface. Incidentally, we kept seeing bright blue light generation at the surface of the disk through our measurements, which is a strong indication of the second harmonic generation at the surface. The sensitivity of the disk for any sensing application can also be improved using this structure, because of the higher light-surface interaction. The novel structure we made can be used for different applications. The surface of the rib disk we developed has a lot more

interaction with the light propagating in the disk, so the surface-mode interaction in this structure is higher than normal disks. This can mean better sensitivity for particle sensing and second harmonic generations since SHG happens at the surface in silica.

Bibliography

[1] Cheng Zhang, Tao Ling, Sung-Liang Chen, and L Jay Guo. Ultrabroad bandwidth and highly sensitive optical ultrasonic detector for photoacoustic imaging. *ACS Photonics*, 1(11):1093–1098, 2014.

[2] Pascal Del'Haye, Albert Schliesser, Olivier Arcizet, Tom Wilken, Ronald Holzwarth, and Tobias J Kippenberg. Optical frequency comb generation from a monolithic microresonator. *Nature*, 450(7173):1214–1217, 2007.

[3] Young-Shin Park and Hailin Wang. Resolved-sideband and cryogenic cooling of an optomechanical resonator. *Nature physics*, 5(7):489–493, 2009.

[4] Ivan S Grudinin, Andrey B Matsko, and Lute Maleki. Brillouin lasing with a caf 2 whispering gallery mode resonator. *Physical review letters*, 102(4):043902, 2009.

[5] Xuyang Zhao, Zhihe Guo, Yi Zhou, Junhong Guo, Zhiran Liu, Yuxiang Li, Man Luo, and Xiang Wu. Optical whispering-gallery-mode microbubble sensors. *Micromachines*, 13(4):592, 2022.

[6] Saeed Farajollahi, Zhiwei Fang, Jintian Lin, Shahin Honari, Ya Cheng, and Tao Lu. Multimode perturbation modeling for cavity polygon and star modes. *Physical Review A*, 108(3):033520, 2023.

[7] Tao Lu, Hansuek Lee, Tong Chen, Steven Herchak, Ji-Hun Kim, Scott E Fraser, Richard C Flagan, and Kerry Vahala. High sensitivity nanoparticle detection using optical microcavities. *Proceedings of the National Academy of Sciences*, 108(15):5976–5979, 2011.

[8] Dengpeng Yuan, Ying Dong, Yujin Liu, and Tianjian Li. Mach-zehnder interferometer biochemical sensor based on silicon-on-insulator rib waveguide with large cross section. *Sensors*, 15(9):21500–21517, 2015.

[9] Shahin Honari, Saeed Farajollahi, and Tao Lu. A novel buckle-free large rib microdisk with submicrometer thickness. *Advanced Photonics Research*, 3(11):2200178, 2022.

[10] Shun Fujii and Takasumi Tanabe. Dispersion engineering and measurement of whispering gallery mode microresonator for kerr frequency comb generation. *Nanophotonics*, 9(5):1087–1104, 2020.

[11] Alexander L Gaeta, Michal Lipson, and Tobias J Kippenberg. Photonic-chip-based frequency combs. *nature photonics*, 13(3):158–169, 2019.

[12] Tobias Herr, Victor Brasch, John D Jost, Christine Y Wang, Nikita M Kondratiev, Michael L Gorodetsky, and Tobias J Kippenberg. Temporal solitons in optical microresonators. *Nature Photonics*, 8(2):145–152, 2014.

[13] Gorodetsky M. L. Lugiato L. A., Prati F. and Kippenberg T. J. From the lugiato–lefever equation to microresonator-based soliton kerr frequency combs. *Phil. Trans. R. Soc.*, 2018.

[14] Seung Hoon Lee, Dong Yoon Oh, Qi-Fan Yang, Boqiang Shen, Heming Wang, Ki Youl Yang, Yu-Hung Lai, Xu Yi, Xinbai Li, and Kerry Vahala. Towards visible soliton microcomb generation. *Nature communications*, 8(1):1–8, 2017.

[15] Gwangho Choi, Adley Gin, and Judith Su. Optical frequency combs in aqueous and air environments at visible to near-ir wavelengths. *Optics Express*, 30(6):8690–8699, 2022.

[16] Maxim Karpov, Martin HP Pfeiffer, Junqiu Liu, Anton Lukashchuk, and Tobias J Kippenberg. Photonic chip-based soliton frequency combs covering the biological imaging window. *Nature communications*, 9(1):1146, 2018.

[17] Hansuek Lee, Tong Chen, Jiang Li, Ki Youl Yang, Seokmin Jeon, Oskar Painter, and Kerry J Vahala. Chemically etched ultrahigh-Q wedge-resonator on a silicon chip. *Nature Photonics*, 6(6):369–373, 2012.

[18] Kerry J Vahala. Optical microcavities. *Nature*, 424(6950):839–846, 2003.

[19] DW Vernooy, Vladimir S Ilchenko, H Mabuchi, EW Streed, and HJ Kimble. High-Q measurements of fused-silica microspheres in the near infrared. *Optics Letters*, 23(4):247–249, 1998.

[20] Guoping Lin, Souleymane Diallo, Rémi Henriet, Maxime Jacquot, and Yanne K Chembo. Barium fluoride whispering-gallery-mode disk-resonator with one billion quality-factor. *Optics Letters*, 39(20):6009–6012, 2014.

[21] Rémi Henriet, Guoping Lin, Aurélien Coillet, Maxime Jacquot, Luca Furfaro, Laurent Larger, and Yanne K Chembo. Kerr optical frequency comb generation in strontium fluoride whispering-gallery mode resonators with billion quality factor. *Optics Letters*, 40(7):1567–1570, 2015.

[22] Lue Wu, Heming Wang, Qifan Yang, Qing-xin Ji, Boqiang Shen, Chengying Bao, Maodong Gao, and Kerry Vahala. Greater than one billion Q factor for on-chip microresonators. *Optics Letters*, 45(18):5129–5131, 2020.

[23] Bahram Jalali and Sasan Fathpour. Silicon photonics. *Journal of lightwave technology*, 24(12):4600–4615, 2006.

[24] AJ Ikushima, T Fujiwara, and K Saito. Silica glass: A material for photonics. *Journal of Applied Physics*, 88(3):1201–1213, 2000.

[25] Wenyan Yu, Wei C Jiang, Qiang Lin, and Tao Lu. Cavity optomechanical spring sensing of single molecules. *Nature communications*, 7(1):1–9, 2016.

[26] Frank Vollmer and Stephen Arnold. Whispering-gallery-mode biosensing: label-free detection down to single molecules. *Nature methods*, 5(7):591–596, 2008.

[27] Tobias J Kippenberg, Ronald Holzwarth, and Scott A Diddams. Microresonator-based optical frequency combs. *Science*, 332(6029):555–559, 2011.

[28] Th Udem, Ronald Holzwarth, and Theodor W Hänsch. Optical frequency metrology. *Nature*, 416(6877):233–237, 2002.

[29] Wenjing Liu, You-Ling Chen, Shui-Jing Tang, Frank Vollmer, and Yun-Feng Xiao. Nonlinear sensing with whispering-gallery mode microcavities: from label-free detection to spectral fingerprinting. *Nano Letters*, 21(4):1566–1575, 2020.

[30] Xu Yi, Qi-Fan Yang, Ki Youl Yang, Myoung-Gyun Suh, and Kerry Vahala. Soliton frequency comb at microwave rates in a high-Q silica microresonator. *Optica*, 2(12):1078–1085, 2015.

[31] Liron Stern, Jordan R Stone, Songbai Kang, Daniel C Cole, Myoung-Gyun Suh, Connor Fredrick, Zachary Newman, Kerry Vahala, John Kitching, Scott A Diddams, et al. Direct kerr frequency comb atomic spectroscopy and stabilization. *Science advances*, 6(9):eaax6230, 2020.

[32] Anatoliy A. Savchenkov, Andrey B. Matsko, Dmitry Strekalov, Makan Mohageg, Vladimir S. Ilchenko, and Lute Maleki. Low threshold optical oscillations in a whispering gallery mode CaF_2 resonator. *Phys. Rev. Lett.*, 93:243905, Dec 2004.

[33] TJ Kippenberg, SM Spillane, and KJ Vahala. Kerr-nonlinearity optical parametric oscillation in an ultrahigh-Q toroid microcavity. *Physical review letters*, 93(8):083904, 2004.

[34] Imad H Agha, Yoshitomo Okawachi, Mark A Foster, Jay E Sharping, and Alexander L Gaeta. Four-wave-mixing parametric oscillations in dispersion-compensated high-Q silica microspheres. *Physical Review A*, 76(4):043837, 2007.

[35] Ki Youl Yang, Katja Beha, Daniel C Cole, Xu Yi, Pascal Del'Haye, Hansuek Lee, Jiang Li, Dong Yoon Oh, Scott A Diddams, Scott B Papp, et al. Broadband dispersion-engineered microresonator on a chip. *Nature Photonics*, 10(5):316–320, 2016.

[36] Tong Chen, Hansuek Lee, and Kerry J Vahala. Thermal stress in silica-on-silicon disk resonators. *Applied Physics Letters*, 102(3):031113, 2013.

[37] Lord Rayleigh O.M. F.R.S. Cxii. the problem of the whispering gallery. *The London, Edinburgh, and Dublin Philosophical Magazine and Journal of Science*, 20(120):1001–1004, 1910.

[38] Lord Rayleigh. Ix. further applications of bessel's functions of high order to the whispering gallery and allied problems. *The London, Edinburgh, and Dublin Philosophical Magazine and Journal of Science*, 27(157):100–109, 1914.

[39] A. Ashkin and J. M. Dziedzic. Observation of resonances in the radiation pressure on dielectric spheres. *Phys. Rev. Lett.*, 38:1351–1354, Jun 1977.

[40] DK Armani, TJ Kippenberg, SM Spillane, and KJ Vahala. Ultra-high-Q toroid microcavity on a chip. *Nature*, 421(6926):925–928, 2003.

[41] Tetsuya Nishiguchi, Hidehiko Nonaka, Shingo Ichimura, Yoshiki Morikawa, Mitsuru Kekura, and Masaharu Miyamoto. High-quality sio 2 film formation by highly concentrated ozone gas at below 600° c. *Applied physics letters*, 81(12):2190–2192, 2002.

[42] Chris Yang and John Pham. Characteristic study of silicon nitride films deposited by lpcvd and pecvd. *Silicon*, 10:2561–2567, 2018.

[43] Cheng Wang, Mian Zhang, and Marko Lončar. High-q lithium niobate microcavities and their applications. In *Ultra-High-Q Optical Microcavities*, pages 1–35. World Scientific, 2021.

[44] Andrey B Matsko and Vladimir S Ilchenko. Optical resonators with whispering-gallery modes-part I: basics. *IEEE Journal of selected topics in quantum electronics*, 12(1):3–14, 2006.

[45] Frank Vollmer and Deshui Yu. *Optical Whispering Gallery Modes for Biosensing*. Springer, 2020.

[46] S Honari, S Haque, and Tao Lu. Fabrication of ultra-high Q silica microdisk using chemo-mechanical polishing. *Applied Physics Letters*, 119(3):031107, 2021.

[47] Xingchen Ji, Felippe AS Barbosa, Samantha P Roberts, Avik Dutt, Jaime Cardenas, Yoshitomo Okawachi, Alex Bryant, Alexander L Gaeta, and Michal Lipson. Ultra-low-loss on-chip resonators with sub-milliwatt parametric oscillation threshold. *Optica*, 4(6):619–624, 2017.

[48] Min Wang, Rongbo Wu, Jintian Lin, Jianhao Zhang, Zhiwei Fang, Zhifang Chai, and Ya Cheng. Chemo-mechanical polish lithography: a pathway to low loss

large-scale photonic integration on lithium niobate on insulator. *Quantum Engineering*, 1(1):e9, 2019.

[49] Matthew Borselli, Kartik Srinivasan, Paul E Barclay, and Oskar Painter. Rayleigh scattering, mode coupling, and optical loss in silicon microdisks. *Applied Physics Letters*, 85(17):3693–3695, 2004.

[50] Shancheng Yang, Yue Wang, and Handong Sun. Advances and prospects for whispering gallery mode microcavities. *Advanced Optical Materials*, 3(9):1136–1162, 2015.

[51] SM Spillane, TJ Kippenberg, KJ Vahala, KW Goh, E Wilcut, and HJ Kimble. Ultrahigh-Q toroidal microresonators for cavity quantum electrodynamics. *Physical Review A*, 71(1):013817, 2005.

[52] Lu Cai, Junyao Pan, and Sheng Hu. Overview of the coupling methods used in whispering gallery mode resonator systems for sensing. *Optics and Lasers in Engineering*, 127:105968, 2020.

[53] Monica Agarwal and Iwao Teraoka. Whispering gallery mode dip sensor for aqueous sensing. *Analytical chemistry*, 87(20):10600–10604, 2015.

[54] J Cheung Knight, G Cheung, F Jacques, and TA Birks. Phase-matched excitation of whispering-gallery-mode resonances by a fiber taper. *Optics letters*, 22(15):1129–1131, 1997.

[55] ML Gorodetsky and VS Ilchenko. High-q optical whispering-gallery microresonators: precession approach for spherical mode analysis and emission patterns with prism couplers. *Optics Communications*, 113(1-3):133–143, 1994.

[56] Arturo Bianchetti, Alejandro Federico, Serge Vincent, Sivaraman Subramanian, and Frank Vollmer. Refractometry-based air pressure sensing using glass microspheres as high-q whispering-gallery mode microresonators. *Optics Communications*, 394:152–156, 2017.

[57] Leilei Shi, Tao Zhu, Dongmei Huang, Min Liu, Ming Deng, and Wei Huang. In-fiber whispering-gallery-mode resonator fabricated by femtosecond laser micromachining. *Optics Letters*, 40(16):3770–3773, 2015.

[58] Ping Zhang, Youlei Ding, and Yufei Wang. Asymmetrical microring resonator based on whispering gallery modes for the detection of glucose concentration. *Optik*, 171:642–647, 2018.

[59] Niranjan M Hanumegowda, Caleb J Stica, Bijal C Patel, Ian White, and Xudong Fan. Refractometric sensors based on microsphere resonators. *Applied Physics Letters*, 87(20), 2005.

[60] Max Born, Emil Wolf, A. B. Bhatia, P. C. Clemmow, D. Gabor, A. R. Stokes, A. M. Taylor, P. A. Wayman, and W. L. Wilcock. *Principles of Optics: Electromagnetic Theory of Propagation, Interference and Diffraction of Light*. Cambridge University Press, 7 edition, 1999.

[61] Jiyang Ma, Longfu Xiao, Jiaxin Gu, Hao Li, Xinyu Cheng, Guangqiang He, Xiaoshun Jiang, and Min Xiao. Visible kerr comb generation in a high-q silica microdisk resonator with a large wedge angle. *Photonics Research*, 7(5):573–578, 2019.

[62] C. Z. Tan. Determination of refractive index of silica glass for infrared wavelengths by ir spectroscopy. *J. Non-Cryst. Solids*, 223:158–163, 1998.

[63] I. H. Malitson. Interspecimen comparison of the refractive index of fused silica. *J. Opt. Soc. Am*, 55, 1965.

[64] Scott B Papp, Katja Beha, Pascal Del'Haye, Franklyn Quinlan, Hansuek Lee, Kerry J Vahala, and Scott A Diddams. Microresonator frequency comb optical clock. *Optica*, 1(1):10–14, 2014.

[65] Philippe Grelu and Nail Akhmediev. Dissipative solitons for mode-locked lasers. *Nature photonics*, 6(2):84–92, 2012.

[66] Zheng Gong, Alexander Bruch, Mohan Shen, Xiang Guo, Hojoong Jung, Linran Fan, Xianwen Liu, Liang Zhang, Junxi Wang, Jinmin Li, et al. High-fidelity cavity soliton generation in crystalline aln micro-ring resonators. *Optics letters*, 43(18):4366–4369, 2018.

[67] Victor Brasch, Michael Geiselmann, Tobias Herr, Grigoriy Lihachev, Martin HP Pfeiffer, Michael L Gorodetsky, and Tobias J Kippenberg. Photonic chip–based optical frequency comb using soliton cherenkov radiation. *Science*, 351(6271):357–360, 2016.

[68] Yang He, Qi-Fan Yang, Jingwei Ling, Rui Luo, Hanxiao Liang, Mingxiao Li, Boqiang Shen, Heming Wang, Kerry Vahala, and Qiang Lin. Self-starting bichromatic $LiNbO_3$ soliton microcomb. *Optica*, 6(9):1138–1144, 2019.

[69] Daoxin Dai and John E Bowers. Novel concept for ultracompact polarization splitter-rotator based on silicon nanowires. *Optics express*, 19(11):10940–10949, 2011.

[70] Govind Agrawal. *Nonlinear Fiber Optics (Fifth Edition)*. Academic Press, 2013.

[71] Lokenath Debnath and Lokenath Debnath. The nonlinear schrödinger equation and solitary waves. *Nonlinear Partial Differential Equations for Scientists and Engineers*, pages 535–577, 2012.

[72] AB Matsko, AA Savchenkov, W Liang, VS Ilchenko, D Seidel, and L Maleki. Mode-locked kerr frequency combs. *Optics letters*, 36(15):2845–2847, 2011.

[73] Martin D Baaske, Matthew R Foreman, and Frank Vollmer. Single-molecule nucleic acid interactions monitored on a label-free microcavity biosensor platform. *Nature Nanotechnology*, 9(11):933, 2014.

[74] Tobias J Kippenberg and Kerry J Vahala. Cavity optomechanics: back-action at the mesoscale. *Science*, 321(5893):1172–1176, 2008.

[75] AJ Campillo, JD Eversole, and HB Lin. Cavity quantum electrodynamic enhancement of stimulated emission in microdroplets. *Physical Review Letters*, 67(4):437, 1991.

[76] Vladimir S Ilchenko, Anatoliy A Savchenkov, Andrey B Matsko, and Lute Maleki. Nonlinear optics and crystalline whispering gallery mode cavities. *Physical Review Letters*, 92(4):043903, 2004.

[77] Jiang Li, Hansuek Lee, Tong Chen, and Kerry J Vahala. Characterization of a high coherence, brillouin microcavity laser on silicon. *Optics Express*, 20(18):20170–20180, 2012.

[78] Michael L Gorodetsky, Andrew D Pryamikov, and Vladimir S Ilchenko. Rayleigh scattering in high-Q microspheres. *Journal of the Optical Society of America B*, 17(6):1051–1057, 2000.

[79] Dae-Gon Kim, Sangyoon Han, Joonhyuk Hwang, In Hwan Do, Dongin Jeong, Ji-Hun Lim, Yong-Hoon Lee, Muhan Choi, Yong-Hee Lee, Duk-Yong Choi, et al.

Universal light-guiding geometry for on-chip resonators having extremely high Q-factor. *Nature Communications*, 11(1):1–7, 2020.

[80] R. Wu, J. Zhang, N. Yao, W. Fang, L. Qiao, Z. Chai, J. Lin, and Y. Cheng. Lithium niobate micro-disk resonators of quality factors above 10^7. *Optics Letters*, 43(17):4116–4119.

[81] GW Trucks, Krishnan Raghavachari, GS Higashi, and YJ Chabal. Mechanism of HF etching of silicon surfaces: A theoretical understanding of hydrogen passivation. *Physical Review Letters*, 65(4):504, 1990.

[82] H Rokhsari, SM Spillane, and KJ Vahala. Loss characterization in microcavities using the thermal bistability effect. *Applied Physics Letters*, 85(15):3029–3031, 2004.

[83] D Ganta, EB Dale, and AT Rosenberger. Measuring sub-nm adsorbed water layer thickness and desorption rate using a fused-silica whispering-gallery microresonator. *Measurement Science and Technology*, 25(5):055206, 2014.

[84] George M. Hale and Marvin R. Querry. Optical constants of water in the 200-nm to 200-μm wavelength region. *Applied Optics*, 12(3):555–563, Mar 1973.

[85] S. Forstner, S. Prams, J. Knittel, E. D. van Ooijen, J. D. Swaim, G. I. Harris, A. Szorkovszky, W. P. Bowen, and H. Rubinsztein-Dunlop. Cavity optomechanical magnetometer. *Phys. Rev. Lett.*, 108:120801, Mar 2012.

[86] Theodore R. Tauchert. Thermally Induced Flexure, Buckling, and Vibration of Plates. *Applied Mechanics Reviews*, 44(8):347–360, 08 1991.

[87] Markus Aspelmeyer, Tobias J Kippenberg, and Florian Marquardt. Cavity optomechanics. *Reviews of Modern Physics*, 86(4):1391, 2014.

[88] Arthur Nitkowski, Long Chen, and Michal Lipson. Cavity-enhanced on-chip absorption spectroscopy using microring resonators. *Optics express*, 16(16):11930–11936, 2008.

[89] Myoung-Gyun Suh and Kerry J Vahala. Soliton microcomb range measurement. *Science*, 359(6378):884–887, 2018.

[90] Yang Sun, Jiayang Wu, Mengxi Tan, Xingyuan Xu, Yang Li, Roberto Morandotti, Arnan Mitchell, and David J Moss. Applications of optical microcombs. *Advances in Optics and Photonics*, 15(1):86–175, 2023.

[91] Qi-Fan Yang, Boqiang Shen, Heming Wang, Minh Tran, Zhewei Zhang, Ki Youl Yang, Lue Wu, Chengying Bao, John Bowers, Amnon Yariv, et al. Vernier spectrometer using counterpropagating soliton microcombs. *Science*, 363(6430):965–968, 2019.

[92] Jian-Ting Li, Bing Chang, Jun-Ting Du, Teng Tan, Yong Geng, Heng Zhou, Yu-Pei Liang, Hao Zhang, Guo-Feng Yan, Ling-Mei Ma, et al. Coherently parallel fiber-optic distributed acoustic sensing using dual kerr soliton microcombs. *Science Advances*, 10(3):eadf8666, 2024.

[93] Michael Kues, Christian Reimer, Joseph M Lukens, William J Munro, Andrew M Weiner, David J Moss, and Roberto Morandotti. Quantum optical microcombs. *Nature Photonics*, 13(3):170–179, 2019.

[94] Steven Miller, Kevin Luke, Yoshitomo Okawachi, Jaime Cardenas, Alexander L Gaeta, and Michal Lipson. On-chip frequency comb generation at visible wavelengths via simultaneous second-and third-order optical nonlinearities. *Optics Express*, 22(22):26517–26525, 2014.

[95] AA Savchenkov, AB Matsko, W Liang, VS Ilchenko, D Seidel, and L Maleki. Kerr combs with selectable central frequency. *Nature Photonics*, 5(5):293–296, 2011.

[96] Shuangyou Zhang, Toby Bi, George N Ghalanos, Niall P Moroney, Leonardo Del Bino, and Pascal Del'Haye. Dark-bright soliton bound states in a microresonator. *Physical Review Letters*, 128(3):033901, 2022.

[97] YuanYao Lin and Ray-Kuang Lee. Dark-bright soliton pairs in nonlocal nonlinear media. *Optics Express*, 15(14):8781–8786, 2007.

[98] SA Gredeskul and Yu S Kivshar. Generation of dark solitons in optical fibers. *Physical review letters*, 62(8):977, 1989.